1   High-resolution Biological Net Community Production in the Pacific-influenced Arctic as

2   Constrained by O_2/Ar and O_2/N_2 Observations

3   Haley Cynar[1], Lauren W. Juranek[1], Calvin W. Mordy[2,3], David Strausz[2,3], Shaun Bell[3]

4   [1] College of Earth, Ocean, and Atmospheric Sciences, Oregon State University, Corvallis, USA

5   [2] Cooperative Institute for Climate, Ocean, and Ecosystem Studies, University of Washington,

6   Seattle, USA

7   [3] Pacific Marine Environmental Laboratory, National Oceanic and Atmospheric Administration,

8   Seattle, USA

9

10   ORCID:

11   (HC) https://orcid.org/0000-0003-0609-5226

12   (LWJ) https://orcid.org/0000-0002-4922-8263

13   (CWM) https://orcid.org/0000-0002-3674-7072

14

15   Correspondence: cynarh@oregonstate.edu

16   Running head: NCP in the Pacific Arctic

17   Keywords: O_2/Ar, O_2/N_2, dissolved gases, gas tension device, primary productivity, net

18   community production, Pacific Arctic

1

19 **Abstract**

20   Spatial and temporal patterns of primary productivity in the Arctic are expected to change

21 with warming-associated changes in ice cover and stratification, yet productivity measurements

22 are historically spatially and temporally limited. Over the last two decades, an approach that uses

23 measurement of dissolved oxygen/argon ratios (O_2/Ar) from a vessel's underway seawater

24 system has emerged as an established method to assess net community production (NCP) rates

25 with high spatial and/or temporal resolution. More recently, the measurement of oxygen/nitrogen

26 ratios (O_2/N_2) with a gas tension device (GTD) and optode have been piloted in underway

27 settings to provide comparable NCP estimates. The GTD/optode approach has several

28 advantages: instrumentation is small, inexpensive, and suitable for autonomous deployments;

29 however, dissimilarity in solubility between O_2 and N_2 makes this tracer pair less accurate than

30 O_2/Ar. We conducted a side-by-side ship-based comparison of a GTD/optode and EIMS in the

31 Pacific Arctic during one of the North Pacific Research Board Integrated Ecosystem Research

32 Program cruises in 2019. NCP from O_2/Ar and O_2/N_2 approaches were coherent throughout this

33 cruise, with median mixed layer integrated NCP of 9.3 ± 2.8 and 7.9 ± 3.2 mmol O_2 m^{-2} day^{-1},

34 respectively. The range of NCP was large, from less than zero to >100 mmol O_2 m^{-2} day^{-1}, with

35 some of the largest NCP estimates measured at well-established hotspots in the Pacific Arctic.

36 While O_2/Ar and O_2/N_2 largely tracked each other, deviations were observed, principally in the

37 Bering Sea where wind-induced bubbles were a primary driver, while a combination of

38 temperature and wind drove differences over the majority of the cruise. The GTD/optode can be

39 used to enhance spatial and temporal coverage of NCP measurements, yet the uncertainty makes

40 this approach better-suited to regions with higher overall rates of NCP, while regions near-

2

41   equilibrium may result in unacceptably high uncertainty. Additionally, the GTD/optode is reliant

42   on well-calibrated oxygen observations, a potential challenge if autonomously deployed.

43   **1.   Introduction**

44   The Arctic Ocean is changing at an unprecedented rate: the thirteen lowest minimum sea

45   ice extents in the satellite record have all occurred between 2007 and 2020, while the trend in

46   September sea ice extent has been declining by 13.3% per decade over the period 1979-2014,

47   relative to the mean September sea ice extent from 1981-2010 (Serreze and Stroeve 2015;

48   Stroeve and Meier 2018; Andersen et al. 2020). In some of the most impacted regions of the

49   Arctic Ocean, including the Chukchi and western Beaufort seas, the ice season duration has been

50   declining by an average of 2.8 days per year from 1979/1980 to 2010/2011 (Stammerjohn et al.

51   2012). This rapid decline in sea ice impacts the physical environment in many ways: increased

52   exchange of heat and gases (CO_2) across the air-sea boundary (Anderson and Kaltin 2001;

53   Carmack et al. 2015; Danielson et al. 2020; DeGrandpre et al. 2020), enhanced wind fetch across

54   open water that results in greater waves (Thomson and Rogers 2014), and greater stratification

55   from low-salinity meltwater (Toole et al. 2010). Stronger stratification limits vertical mixing,

56   which in turn limits surface nutrient supply, a fundamental requirement for photosynthesis

57   (Semiletov et al. 2004; Carmack and Wassmann 2006; Song et al. 2021).

58   The impact of these physical changes on primary productivity is uncertain, with

59   hypotheses for both increasing and decreasing production based on nutrient and light availability.

60   Remote sensing studies have indicated an increase in primary production, driven by sea ice loss

61   and reduction in light limitation (Arrigo et al. 2008; Tremblay et al. 2011; Arrigo and van Dijken

62   2015), although these studies acknowledge a requirement for increased nutrient flux to maintain

63   production. This influx of nutrients could be sustained by increased supply from adjacent

3

64   subpolar seas. Nitrate replenishment is highly variable in the eastern Chukchi Sea (Mordy et al.

65   2020), an inflow shelf that serves as a gateway to the Arctic where nutrient-rich Pacific-origin

66   water shoals through Bering Strait onto the Chukchi shelf. Due to this influx, inflow shelves are

67   expected to be most impacted by enhanced nutrient supply from neighboring seas (Tremblay and

68   Gagnon 2009; Tremblay et al. 2015; Lewis et al. 2020). Alternatively, potential increases in

69   cloud cover are expected to decrease production (Bélanger et al. 2013), while increased delivery

70   of freshwater and dissolved constituents from terrestrial snow, ice, and permafrost melt via

71   Arctic rivers will impact nutrients, stratification, and organic matter in coastal regions with

72   variable results (Carmack and Wassmann 2006). Overall, a melting Arctic Ocean will alter

73   surface light and nutrient availability on a seasonal basis, effectively controlling phytoplankton

74   growth, and thus carbon and energy cycling in Arctic marine food webs (Grebmeier et al. 2006;

75   Harada 2016). These shifts are best understood through a multidisciplinary approach, as with the

76   North Pacific Research Board Arctic Integrated Ecosystem Research Program

77   (https://www.nprb.org/arctic-program; Baker et al. 2020, 2022, this issue).

78   While remote sensing approaches are one of the best tools for providing spatially and

79   temporally resolved estimates of marine primary productivity, passive measurements (e.g., ocean

80   color) are often limited in some seasons and regions of the Arctic due to cloud cover, especially

81   during the late ice-free season (August-October) when physical system changes exhibit strong

82   trends. Additionally, satellite-based estimates of net community productivity (NCP) are not yet

83   widely available in the Pacific Arctic region. An important productivity metric, NCP is defined

84   as the total community photosynthesis less both algal and heterotrophic respiration, and is

85   considered to be an estimate of the maximum organic carbon available to be exported out of the

86   surface ocean, with implications for the ecosystem, fisheries, carbon budgets, and climate

4

87   modeling (Wassmann and Reigstad 2011). Since biological production in shallow, marginal seas

88   like the Chukchi can be dynamic, with patchy and short-lived phytoplankton blooms (Juranek et

89   al. 2019), higher resolution methods are needed to capture sporadic and spatially-variable

90   processes in the field and to understand potential drivers of these patterns.

91   In the last two decades, a number of studies have shown the utility of high-resolution

92   observations of surface ocean dissolved oxygen/argon (O_2/Ar) gas ratios to constrain NCP at

93   spatial and or temporal scales that are not accessible with traditional incubation methods (e.g.,

94   Hamme et al., 2012; Eveleth et al., 2017, Juranek et al., 2019). High-resolution O_2/Ar can be

95   obtained continuously in surface seawater using an equilibrated inlet mass spectrometer (EIMS)

96   (Cassar et al. 2009). Since Ar is an inert gas that is not affected by biology but behaves similarly

97   to O_2 with respect to physical forcing, it can be used to isolate the biological effects driving O_2

98   (Benson and Krause 1984; Craig and Hayward 1987). The ratio of biologically and physically

99   controlled O_2 to physically controlled Ar therefore can be used to provide an estimate of net

100   biological oxygen production (Kaiser et al. 2005). The O_2/Ar ratio is insensitive to changes due

101   to warming, cooling, and wind-driven bubble exchange and injection due to the similarity in

102   physical properties between oxygen and argon. When O_2/Ar measurements are combined with a

103   mass-balance budget for the surface ocean, spatially resolved estimates of NCP can be produced

104   (e.g., Stanley et al. 2010; Hamme et al. 2012; Eveleth et al. 2017; Teeter et al. 2018).

105   Another related, but less frequently used approach for obtaining NCP is to use

106   observations of the O_2/N_2 ratio in seawater. Similar to the case with O_2/Ar, N_2 is used to track

107   abiotic forcing. However, while O_2 and Ar are an ideal tracer pair due to the similar solubility of

108   these gases, the solubility of N_2 is less similar to O_2, and is impacted differently by both physical

5

109   forcing (i.e., warming, cooling, and bubbles) and, at times, biological influences (i.e., nitrogen

110   fixation and denitrification).

111   The O_2/N_2 method was previously described by Emerson et al. (2002), who used

112   observations from a mooring in the subtropical North Pacific to estimate net biological oxygen

113   production. The approach involves measuring total gas pressure as well as pO_2 in seawater with a

114   GTD and O_2 sensor, respectively, with assumptions about less prevalent gases to estimate the

115   amount of dissolved N_2. Because of the reliance on O_2 to calculate N_2, the approach requires

116   accurate dissolved O_2 concentrations (Emerson et al., 2002).

117   GTD measurements were first tested on moorings (McNeil et al. 1995) and have since

118   been broadly applied (Emerson et al. 2002, 2008, 2019; Weeding and Trull 2014; Trull et al.

119   2019), while continuous shipboard GTD measurements have also been made to estimate O_2/N_2-

120   based net biological oxygen production (McNeil et al. 2005). Recently, Izett and Tortell (2020)

121   introduced a GTD and optode configuration (Pressure of In Situ Gases Instrument, or PIGI) for

122   deployment on underway systems, with initial data collection in the northeast Pacific and

123   Canadian Arctic oceans.

124   While O_2/N_2-based net biological oxygen estimates are subject to greater biases and

125   uncertainties due to the dissimilarities in physical forcing of O_2 and N_2, there are also key

126   advantages to the approach. The GTD/optode system is small, submersible, and low-cost, with

127   potential for autonomous use, whereas the EIMS involves a more expensive, ship-based mass

128   spectrometer that requires supervision.

129   Here, we compare underway O_2/N_2 to the more established O_2/Ar method (Stanley et al.

130   2010; Hamme et al. 2012; Lockwood et al. 2012; Eveleth et al. 2014) to (1) evaluate the utility of

6

131   the O_2/N_2 approach for autonomous underway applications, (2) quantify spatial variability in

132   NCP, and (3) evaluate potential physical drivers of NCP in this region of the Pacific Arctic.

133   *1.1.   Basis of O_2/Ar and O_2/N_2 approach*

134   Biological O_2 production can be stoichiometrically related to the net inventory of organic

135   carbon produced through the balance of community photosynthesis and respiration, i.e.: CO_2 +

136     $H_2O \longleftrightarrow$ organic matter + O_2. As is evident from this expression, net biological oxygen

137   increases (decreases) due to photosynthesis (respiration) in a given parcel of water. However,

138   background concentrations of O_2 in surface seawater are set by temperature- and salinity-

139   controlled solubility (Garcia and Gordon, 1992). Therefore, deviations from solubility

140   equilibrium, identified by the dissolved gas saturation anomaly of oxygen in the surface ocean:

141     $\Delta O_2 (\%) = 100*([O_2]_{meas}/[O_2]_{sat} - 1)$ (1)

142   where $[O_2]_{meas}$ is the measured oxygen concentration and $[O_2]_{sat}$ is the equilibrium oxygen

143   solubility, are due to a combination of recent biological and physical forcing. For example, a

144   recent water column warming of 3°C (e.g., from 10° to 13°C) without sufficient time for re-

145   equilibration with the atmosphere would increase ΔO_2 by 6.57% due to the decrease in solubility

146   of O_2 ($[O_2]_{sat}$) with increasing temperature. A positive gas saturation anomaly could also be

147   driven by a source of O_2 (i.e., photosynthesis), which increases $[O_2]_{meas}$. Without an additional

148   tracer gas, it is difficult to identify when positive ΔO_2 are driven by biological production or a

149   combination of physical factors. By simultaneously measuring an abiotic gas such as Ar or N_2 as

150   a tracer of physical saturation changes, the physical and biological components of the ΔO_2 signal

151   can be parsed out. Ar has been widely used as an abiotic tracer alongside O_2 because it is inert

152   and is physically similar to oxygen (Craig and Hayward 1987). Although N_2 has biological

7

153   sources and sinks, the effect of these processes are undetectable given the large N_2 background in

154   surface measurements, making N_2 an effective tracer of physical processes (Emerson et al.

155   2002). With Ar and N_2 serving as proxies for physical gas saturation, the normalization of ΔO_2

156   relative to either gas yields a tracer of the net biological oxygen saturation (Kaiser et al., 2005).

157   The physical differences between N_2 and O_2 are significantly greater than those between

158   Ar and O_2, so physical forcing (for example, warming or cooling of water masses) is expected to

159   drive slightly different responses in O_2 and N_2, and hence the O_2/N_2 ratio will not be a perfect

160   tracer of net biological O_2 production. Since N_2 makes up 78% of the atmosphere (Glueckauf

161   1951) yet is less soluble in seawater than either O_2 or Ar, the effect of bubble injection increases

162   N_2 saturation significantly more than O_2 or Ar. The effect of temperature change on N_2, in

163   contrast, is smaller than that of O_2 and Ar, which also biases the ratio when temperature change

164   is observed.

165   To account for the physical biases of N_2, Izett et al. (2021) introduced a calculated value,

166   N_2', which more closely approximates a physical analogue of oxygen, improving upon the

167   approximation of net biological oxygen production based on O_2/N_2 in some regions. We explored

168   the utility of this N_2' approach in our study region by comparing O_2/N_2 and O_2/N_2' with O_2/Ar

169   observations.

170   **2.   Methods**

171   In this study, EIMS- and GTD- based estimates of NCP were obtained for a side-by-side

172   comparison on leg 1 of the OS1901 cruise (August 1 to August 24, 2019), part of the North

173   Pacific Research Board's Arctic Integrated Ecosystem Research Program (Baker et al. 2020,

8

174   2022) in the Chukchi and Beaufort Seas, on R/V *Ocean Starr*. Leg 1 of the cruise embarked from

175   Dutch Harbor, AK and ended in Nome, AK.

176   *2.1.   Dissolved O_2 measurements*

177   An Aanderaa optode (4330F) was placed in-line with the GTD in the flowthrough

178   seawater system, which had a nominal intake depth of 3.5 meters. The optode was calibrated

179   from discrete samples that were collected periodically throughout the cruise (n=26), and

180   analyzed using the Winkler method (Carpenter 1965). Upon inspection, 5 of these samples were

181   determined to be outliers (offset $>2\sigma$ from mean or were analyzed in a batch of samples that

182   were subject to analysis error); these outliers were excluded from further analysis. Oxygen gain

183   (Winkler O_2 / optode O_2) was determined with respect to time, temperature, and oxygen

184   concentration, where the best fit linear model of the difference in gain correction as a function of

185   time ($R^2 = 0.58$) was applied to the data (Figure S1, Supplemental Information). This time-based

186   gain correction ranged from 1.034 to 1.051 and is described in the Supplemental Information.

187   *2.2.   EIMS-O_2/Ar*

188   An equilibrated inlet mass spectrometer (EIMS), which consists of a quadrupole mass

189   spectrometer (Pfeiffer PrismaPlus QMG 220) coupled to a system for separation of dissolved

190   gases from seawater, was configured similarly to that described by Cassar et al. (2009). O_2/Ar

191   ratios were continuously measured on surface seawater by the EIMS, where seawater passed

192   through a 40 mesh (0.42 mm) coarse screen into an overflowing cylinder in a sipper system.

193   Seawater near the inflow of this cylinder was pumped through 100 µm and 5 µm filters and then

194   passed through a contactor membrane (3M Liqui-cel MicroModule 0.75 x 1, model G569) with

195   large surface area in which dissolved gases equilibrated. The headspace of gas in this contactor

9

196   membrane was sampled by a fused silica capillary (2 m x .05 mm ID) connected to the

197   quadrupole mass spectrometer. A changeover valve allowed outside air to be admitted for 30

198   minutes every 3 hours. The O_2/Ar in ambient air is considered to be constant, so consistent air

199   measurements throughout the cruise allows for calibration of the seawater O_2/Ar signal to air

200   O_2/Ar to account for potential drift in EIMS measurements over time.

201   The EIMS O_2/Ar ratios were time-averaged into 2.5-minute intervals to yield

202   measurements with average spatial resolution of ca. 0.6 km along the ship transit. EIMS-based

203   O_2/Ar measurements are slightly lagged relative to faster response O_2 optode data due to

204   equilibration and capillary transport time. Using a cross-correlation analysis, an EIMS-to-optode

205   lag of 8.5 minutes was identified, and the EIMS time axis was shifted accordingly to align with

206   the faster response optode data. Bottle samples were collected from the underway seawater

207   stream twice a day and analyzed via a shore-based Thermo 253 Isotope Ratio Mass Spectrometer

208   (IRMS) as in Juranek et al. (2012). Bottle samples were used as a secondary, external accuracy

209   check on air corrected EIMS O_2/Ar. Outliers in the bottle calibrations (offset $>3\sigma$ from mean

210   difference) were observed in frontal regions of rapid O_2/Ar ratio change, and were excluded from

211   comparison because small differences in sampling response time allowed for large offsets

212   between EIMS and bottle O_2/Ar that were inconsistent with the majority of the data. Bottle and

213   EIMS O_2/Ar data were used with paired temperature and salinity to calculate the O_2/Ar

214   saturation anomaly (ΔO_2/Ar) as follows:

215    $\Delta O_2/Ar = 100*[(O_2/Ar)_{meas}/(O_2/Ar)_{sat}-1]$,   (2)

216   where $(O_2/Ar)_{sat}$ refers to the ratio of gases at saturation in seawater and O_2 and Ar solubilities

217   are calculated according to Garcia and Gordon (1992) and Hamme and Emerson (2004),

218   respectively. We observed a consistent, stable offset between EIMS and bottle sample ΔO_2/Ar of

       10

219 -1.33 % (n=34, s.e.m.=0.1%). The discrete bottle sampling occurred at the same sink where the

220 EIMS sipper system was sampling from, such that no difference in warming or potential

221 respiration in the lines (Juranek and Quay 2010) is expected to have led to this difference. A 5%

222 difference in the EIMS total pressure between air and equilibrator measurements was attributed

223 to slight differences in PEEK tubing length; because the gas ratio measurements are affected by

224 total gas pressure in the quadrupole mass spectrometer this difference likely contributed to the

225 offset correction required for $\Delta O_2/Ar$ on this cruise. We adjusted all EIMS data to correct for this

226 offset. See metadata description accompanying archived data at arcticdata.io

227 (doi:10.18739/A2HH6C69V) for further details.

228 *2.3.   GTD-O_2/N_2*

229   The Pro-Oceanus miniTDGP (referred to as GTD) was installed on the flowthrough

230 seawater system to measure total dissolved gas pressure of surface seawater throughout the

231 cruise. This device measures the total dissolved gas pressure across a permeable membrane twice

232 per second. The flow rate of seawater entering the GTD was about 1.2 L min^{-1}, which yielded

233 measurements with a faster response time than the EIMS. The underway seawater was split

234 between the sensor wall (where the TDGP was located) and the EIMS tap, which had a split

235 valve for discrete sampling. Since this TDGP configuration was set up directly in line with the

236 underway seawater (in contrast to the EIMS with a sipper), these measurements were subject to

237 greater noise at times due to bubbles in the seawater line, despite being adjacent to the EIMS

238 seawater sampling location.

239   The GTD measures total dissolved gas pressure in seawater ($P^w_{GTD,}$) expressed as in

240 Equation 3,

11

241    $P^w_{GTD} = P^w_{N2} + P^w_{O2} + P^w_{H20} + P^w_{Ar} + P^w_{CO2}$ (3)

242   where P^w_x refers to the partial pressure of dissolved N_2, O_2, water vapor, Ar, and CO_2 in

243   seawater, respectively. This expression excludes gases with partial pressures less than 20 µatm,

244   which Emerson et al. (2002) showed was a reasonable assumption. P^w_{Ar}, P^w_{CO2}, and P^w_{H2O} are

245   assumed to be at equilibrium with the atmosphere, an assumption that is likely inaccurate, yet

246   expected deviations in these gas concentrations will not strongly affect the calculation due to the

247   small contribution of each of these gases to total dissolved gas pressure. Alternately, the

248   saturation of Ar can be assumed to be equal to N_2 in the calculation based on roughly similar

249   saturations from physical forcing (McNeil et al. 2005). In this study, we assume P^w_{Ar} to be in

250   equilibrium with the atmosphere, but we investigate the impact of these assumptions in Section

251   3.2. The dry air mole fraction of CO_2 in the atmosphere was used in this calculation, where the

252   monthly average pCO_2 in August 2019 at the Point Barrow, AK climate monitoring station was

253   400 ppm (NOAA CMDL, https://www.esrl.noaa.gov/gmd/dv/data/). The partial pressure of CO_2

254   and Ar were calculated based on the mole fraction of each gas in the atmosphere with the

255   relationship in Equation 4:

256    $P^a_i = X_i * (1013.25 - P^a_{H20})$ (4)

257   where P^a_i is the partial pressure of gas (i=CO_2 or Ar), X_i is the fraction of gas in a dry

258   atmosphere, 1013.25 is the standard atmospheric pressure (in mbar) and P^a_{H2O} is the partial

259   pressure of water vapor in the atmosphere (Glueckauf 1951). P^w_{H2O} is assumed to be at saturation

260   in the GTD headspace and is calculated with the formula of Weiss and Price (1980).

261   To calculate the partial pressure of dissolved oxygen, a solubility factor, α_{O2} was calculated with

262   units of mol kg^{-1} mbar^{-1} as follows:

12

263     $\alpha_{O2} = [O_2]_{sat}/(1013.25 - P^a_{H2O}) * X_{O2}$ (5)

264   where the equilibrium saturation concentration of oxygen at each location, $[O_2]_{sat}$, was

265   determined based on the equations of Garcia and Gordon (1992). The 1013.25 term is for

266   standard atmospheric pressure (mbar) and P^a_{H2O} is the partial pressure of water vapor in the

267   atmosphere (in mbar, assumed to be at saturation) and X_{O2} is the mole fraction of O_2 in a dry

268   atmosphere (Glueckauf 1951). This solubility constant, α_{O2}, was then used to calculate the partial

269   pressure of O_2 in the water vapor-saturated headspace of the GTD as in Equation 6,

270     $P^w_{O2} = [O_2]_{meas}/\alpha_{O2}$ (6)

271   where $[O_2]_{meas}$ is the concentration of O_2 measured by the optode, in mol/kg. The P^w_{N2} can then

272   be calculated as (Emerson et al. 2002):

273     $P^w_{N2} = P^w_{GTD} - (1013.25 - P^a_{H20}) * (X_{Ar} + X_{CO2}) - P^w_{H20} - [O_2]_{meas}/\alpha_{O2};$ (7)

274   The P^w_{GTD} data were time-shifted to account for a 1-minute GTD-to-optode lag

275   (determined via a cross-correlation analysis of the entire dataset, see metadata description

276   accompanying archived data for further details; doi:10.18739/A2804XM1W) relative to the

277   faster response Aanderaa optode data, a response time that is within the range of comparable

278   systems (Izett and Tortell 2020). The flow was manually maintained at 1.2 L min^{-1} and flow rate

279   was not recorded. Slight variations in flow may have caused slight variations in the response

280   time but these are not likely to influence our interpretation of the data. From P^w_{N2} and P^w_{O2} as

281   calculated post-P^w_{GTD} lag correction, measured O_2/N_2 ratios were determined.

282   We report O_2/N_2 here in terms of a saturation anomaly ratio comparable to Equation 2:

283     $\Delta O_2/N_2 (\%) = 100 * [(O_2/N_2)_{meas}/(O_2/N_2)_{sat} - 1]$ (8)

13

284   where $(O_2/N_2)_{sat}$ refers to the ratio of gases at saturation in equilibrium with the GTD headspace

285   as calculated by Equation 6 and 7. The gas solubilities are calculated from Garcia and Gordon

286   (1992) and Hamme and Emerson (2004). After calculating the O_2/N_2 ratio, a median residual

287   filter was applied to remove outliers and noise due to in-line bubbles. A moving median was

288   calculated based on a 12-minute window, with residuals outside of 2.4 standard deviations from

289   the mean flagged as outliers. This threshold was determined to exclude less than 5% of the data.

290   This filtered version of O_2/N_2 is used throughout this manuscript and is referred to as noise-

291   filtered (n.f.). See metadata description accompanying archived data at arcticdata.io

292   (doi:10.18739/A2804XM1W) for further details.

293   *2.4.   Comparison of O_2 /Ar and O_2 /N$_2$ data*

294   To assess the difference between O_2/Ar and O_2/N_2 ratios, we calculate the term diff-Δ:

295   diff-Δ (%) = $\Delta O_2/Ar$ - $\Delta O_2/N_2$ (9)

296   Initially, to get more directly comparable $\Delta O_2/Ar$ - $\Delta O_2/N_2$, we tried to account for the dynamic

297   response effects of the EIMS. The EIMS equilibrator uses a contactor membrane that dampens

298   the signal due to the time required for gases to reach equilibrium across the membrane. When

299   calculating diff-Δ, the comparatively slower response of the EIMS relative to the GTD creates

300   data artifacts due to mismatched peaks. In an attempt to account for smearing of signals within

301   the EIMS equilibrator, smoothed versions of $\Delta O_2/N_2$ were calculated, but neither a time filter (as

302   in Hamme et al. 2015), nor a one-sided exponential filter with e-folding time comparable to that

303   described by Cassar et al. (2009) for EIMS system response, closely approximated the smoothing

304   effect of the EIMS contactor membrane. Because of this inability to slow down the GTD

305   observations in a way that was directly comparable to the EIMS we decided to directly compare

14

306   the GTD and EIMS records instead, and to flag areas where rapid changes in O_2/Ar and O_2/N_2

307   caused large diff-Δ that are likely an artifact of differential dynamic responses.

308   *2.5.   NCP calculation*

309   Net community production (NCP) was calculated for $\Delta O_2/Ar$ and $\Delta O_2/N_2$ values by

310   assuming a steady state balance between net biological oxygen production and air-sea gas

311   exchange in the surface mixed layer with no horizontal advection or vertical mixing of water

312   masses (Craig and Hayward 1987; Kaiser et al. 2005; Hamme and Emerson 2006; Stanley et al.

313   2010). When there is physical transport of deeper water to the surface and mixing assumptions

314   are invalidated it is not appropriate to calculate NCP using this steady-state balance (Teeter et al.

315   2018). Diagnosing potential mixing biases using only surface underway data can be challenging,

316   but some characteristics of deeper water that may indicate vertical mixing in the region of this

317   study include elevated salinity coupled with negative $\Delta O_2/Ar$ at the surface, since subsurface

318   waters are typically depleted in oxygen at depth due to respiration, and their salinity is higher

319   due to minimal influence of seasonal ice melt at depth. In this dataset, areas with both a $\Delta O_2/Ar$

320   less than -2% and a surface salinity greater than 32.5 (where the mean surface salinity over the

321   cruise was 30.6, with less than 5% of measurements greater than 32.5) are assumed to be subject

322   to vertical mixing, and are excluded from NCP analysis.

323   NCP based on the surface mass balance (Hendricks et al. 2004; Juranek and Quay 2005)

324   was calculated using Equation 10 with NCP in mmol O_2 m^{-2} day^{-1}:

325    $$NCP=(k_{O2})(O_2)_{sat}(\Delta O_2/[X])/100, \qquad\qquad\qquad (10)$$

326   In Equation 10, k_{O2} is the air-sea gas exchange rate (m day^{-1}), $(O_2)_{sat}$ is the equilibrium saturation

327   of oxygen calculated as described above (mmol m^{-3}), and $\Delta O_2/[X]$ is either $\Delta O_2/Ar$ or $\Delta O_2/N_2$ as

15

328   calculated with Equation 2 or 8. The gas transfer velocity, k_{O2}, is dependent on wind speed and

329   was calculated based on Wanninkhof (2014) using the wind speed weighting technique of Reuer

330   et al. (2007), assuming a constant 20 meter mixed layer depth (MLD). The MLD observed at the

331   time of sampling fluctuated regionally throughout this cruise, with deeper MLDs in the Bering

332   Sea and shallower (<15 meter) MLD in the Chukchi and Beaufort Seas, as determined by the

333   pycnocline depth. The MLD in these areas may have also varied in the weeks prior to sampling,

334   such that an estimate of 20 meters is a reasonable approximation with some uncertainty based on

335   the historical MLD. In areas with shallower MLDs, the assumed 20-meter MLD results in an

336   overestimate of k_{O2} of about 3%, while areas with deeper MLDs result in an underestimate of

337   less than 1% in k_{O2}, biases which propagate into NCP estimates. Three-hourly average

338   directional components of wind speed from NCEP North American Regional Reanalysis

339   (NARR) provided by the NOAA/OAR/ESRL PSL, Boulder, Colorado, USA were used in

340   calculating the gridded wind speed for the 60 days prior to ship observations

341   (https://psl.noaa.gov/).

342   *2.6.   Variables to Assess Physical Gas Saturation*

343   To evaluate potential variables that might correlate with differences in O_2/Ar and O_2/N_2

344   ratios, we compare remotely sensed wind speed and temperature to diff-Δ. The three-hour wind

345   speed from NARR was used in calculating the maximum wind speed over the two preceding

346   weeks, as well as the percent of wind speeds exceeding 10 m s^{-1} over prior weeks. Net

347   temperature change was calculated as the sum of daily sea surface temperature (SST) change 14

348   and 30 days prior to sampling using NOAA High-resolution Blended Analysis of Daily SST and

349   Ice data collocated with the cruise track provided by the NOAA/OAR/ESRL PSL, Boulder,

350   Colorado, USA, from (https://psl.noaa.gov/).

16

351   *2.7. N_2' Calculations*

352   N_2' is a value which approximates a physical analogue of oxygen, and is determined with

353   a model developed by Izett and Tortell (2021) that is based on the historical physical forcing

354   (wind, temperature, atmospheric pressure) in combination with measured N_2 saturation to correct

355   for biases. When using this model in calculating N_2' for this cruise, three-hour average

356   directional components of wind speed and daily atmospheric pressure at mean sea level from

357   NCEP North American Regional Reanalysis (NARR) provided by the NOAA/OAR/ESRL PSL,

358   Boulder, Colorado, USA were used in calculating the historical wind speed and atmospheric

359   pressure collocated with the cruise track for the 90 days prior to ship observations.

360   (https://psl.noaa.gov/). Daily sea surface temperature (SST) based on NOAA High-resolution

361   Blended Analysis of Daily SST and Ice data collocated with the cruise track provided by the

362   NOAA/OAR/ESRL PSL, Boulder, Colorado, USA, from (https://psl.noaa.gov/) was used in

363   modeling historical temperature. Salinity was assumed to remain constant, equal to the salinity

364   measured at cruise sampling, while vertical mixing was ignored in these calculations due to lack

365   of subsurface gas saturation data. The bubble scaling coefficient, β, was set to 0.5 for these

366   calculations. This value was found to be optimal for the Izett and Tortell (2021) dataset, and

367   sensitivity tests were conducted with this dataset that indicated our modeling results did not

368   depend strongly on β.

17

3.   Results and Discussion

3.1.   Spatial patterns

A comparison of spatial distributions of ΔO_2 with $\Delta O_2/Ar$ for OS1901 illustrates how oxygen supersaturation and net biological oxygen supersaturation are related (Figure 1). Note that there are regions (e.g., red circle at 60°N) with strong oxygen supersaturation that were co-located with negative $\Delta O_2/Ar$, suggesting that oxygen supersaturation was purely driven by physical factors (e.g., wind and bubbles or warming). The biological signal opposed this trend, but did not completely compensate for physical effects. In other areas, ΔO_2 was greater than $\Delta O_2/Ar$, suggesting a mix of physical and biological forcing of oxygen supersaturation. The spatial patterns in $\Delta O_2/Ar$ indicated areas of large net biological supersaturation with $\Delta O_2/Ar$ peaks above 30% near the Aleutian arc, in Chirikov Basin and southwest of Point Hope. Regions
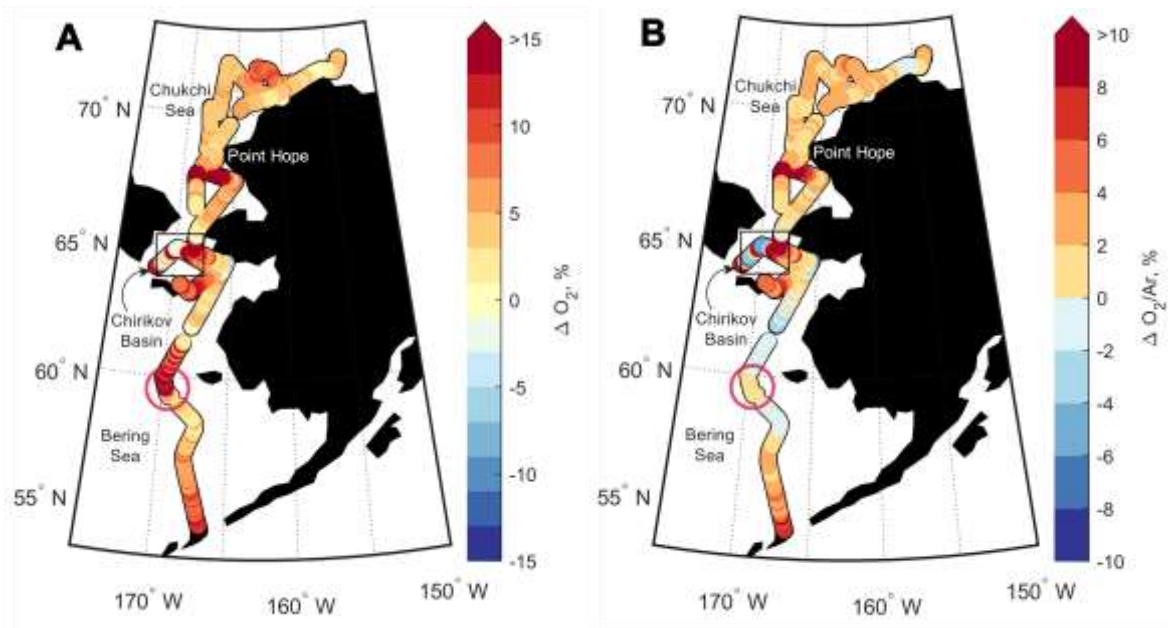

Figure 1: ΔO_2 and $\Delta O_2/Ar$ along the cruise track (scale attenuated to emphasize near-equilibrium trends, note different scales in A and B). These trends in $\Delta O_2/Ar$ are also seen in $\Delta O_2/N_2$ (not shown), with additional noise. The cruise began in Dutch Harbor, AK and ended in Nome, AK. Breaks in the track line were due to gaps in data collection.

18

380   in Chirikov Basin and southwest of Point Hope are established biological hotspots (Grebmeier et

381   al. 2015).

382   In these biological hotspots, elevated underway chlorophyll-a (from a Seabird ECO-FL

383   fluorometer) corresponded with high $\Delta O_2/Ar$ on 3 out of 4 instances (Figure 2). The peak of

384    $\Delta O_2/Ar$ that did not correspond to elevated fluorescence occurred in the region off Point Hope,

385   which was occupied twice (August 11th and August 23rd). While low concentrations of

386   chlorophyll-a were observed during the first occupation, a chlorophyll peak was observed on the

387   later occupation. A mismatch between chlorophyll-a and O_2/Ar is expected at times because of

388   the different residence

389   timescales associated

390   with dissolved gases and

391   chlorophyll production in

392   the surface ocean: the O_2

393   signal from a bloom will

394   take 2-3 weeks to

395   reequilibrate with the

396   atmosphere, whereas

397   chlorophyll biomass can
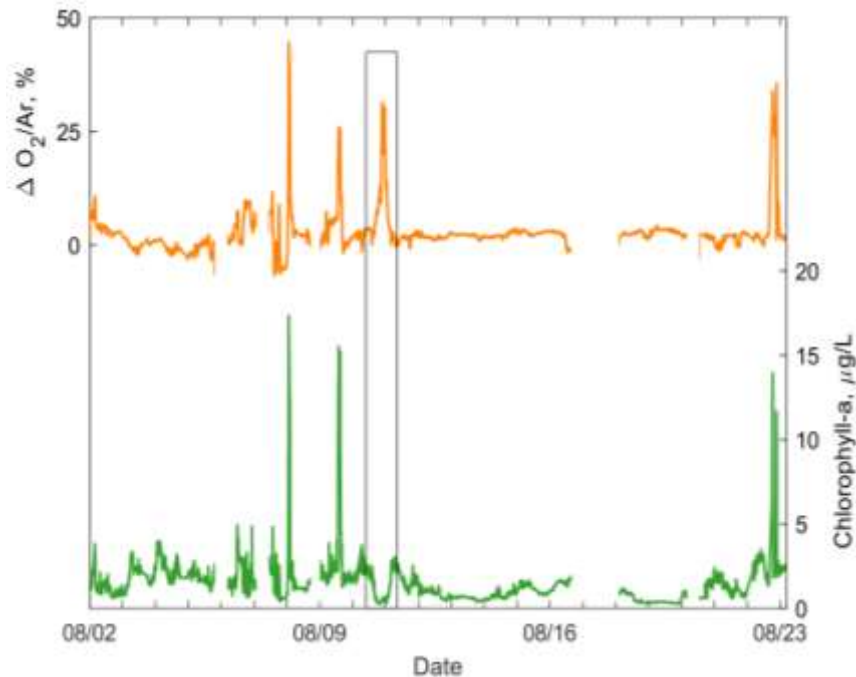
398   sink or be consumed by

Figure 2: Underway measurements of $\Delta O_2/Ar$ and chlorophyll-a based on fluorescence throughout the cruise. Boxed area indicates occupation off of Pt. Hope with low chlorophyll and elevated $\Delta O_2/Ar$.

399   grazers over shorter

400   timescales. Chlorophyll-a data from MODIS-Aqua (NASA Goddard Space Flight Group; Ocean

401   Ecology Laboratory; Ocean Biology Processing Group, https://modis.gsfc.nasa.gov/data/) were

402   sparse in the weeks prior to shipboard measurements, but the edge of a bloom with elevated

19

403   chlorophyll-a was seen off of Point Hope on August 4, 2019, about 7 days prior to shipboard

404   measurements in the same location (not shown). This elevated biological production was

405   indicated in the shipboard O_2/Ar, while the production of chlorophyll-a may have attenuated over

406   a shorter timescale, resulting in low underway fluorescence. In addition, fluorescence can be

407   impacted by photochemical quenching, which can cause fluorescence to diverge from

408   chlorophyll concentrations (the chlorophyll shown in Figure 2 was calculated directly from

409   fluorescence using manufacturer-supplied coefficients). Photochemical quenching could have

410   contributed to the low estimate of chlorophyll on August 11, which was sampled in late

411   afternoon, yet the quenching effect is not expected to fully deplete the detection of chlorophyll

412   observed on this date.

413   In the Bering Sea, there are several regions where ΔO_2 is positive and $\Delta O_2/Ar$ is negative

414   (Figure 1), consistent with physical supersaturation of oxygen in the surface ocean due to both

415   warming water and increased wind speed ($\Delta O_2 > 0$) and net heterotrophic biological activity

416   ($\Delta O_2/Ar < 0$). In Chirikov Basin, $\Delta O_2/Ar$ was variable, with patches of large supersaturation as

417   well as undersaturation that could be attributed to the dynamic nature of water masses mixing in

418   this area (Danielson et al. 2017). The areas with both negative and positive $\Delta O_2/Ar$ in the

419   western part of Chirikov Basin are in significantly colder, saltier, nitrate-rich water (salinity

420   >32.5, NO_3>20 µM from an underway nutrient sensor, data not shown) typical of Anadyr water

421   (Grebmeier et al. 2006). The $\Delta O_2/Ar$ signals here likely reflect a combination of recent vertical

422   mixing of subsurface water with a depleted O_2 signature to the surface and patchy production

423   sparked by high nutrient Anadyr water when light and stratification conditions were favorable. In

424   the majority of the Chukchi Sea, net biological oxygen supersaturation was positive, indicating

20

425   net autotrophy (median $\Delta O_2/Ar$=2% ±2.1%, median absolute deviation=0.8% when excluding

426   biological hotspots where $\Delta O_2/Ar > 5\%$).

427   *3.2.   EIMS-GTD Comparison*

428   There was relative agreement between $\Delta O_2/N_2$ and $\Delta O_2/Ar$ for OS1901, with both ratios

429   indicating net biological oxygen supersaturation for the majority of the cruise (Figure 3A).

430   Throughout the cruise, $\Delta O_2/N_2$ was slightly less than $\Delta O_2/Ar$, yet in areas of large biological
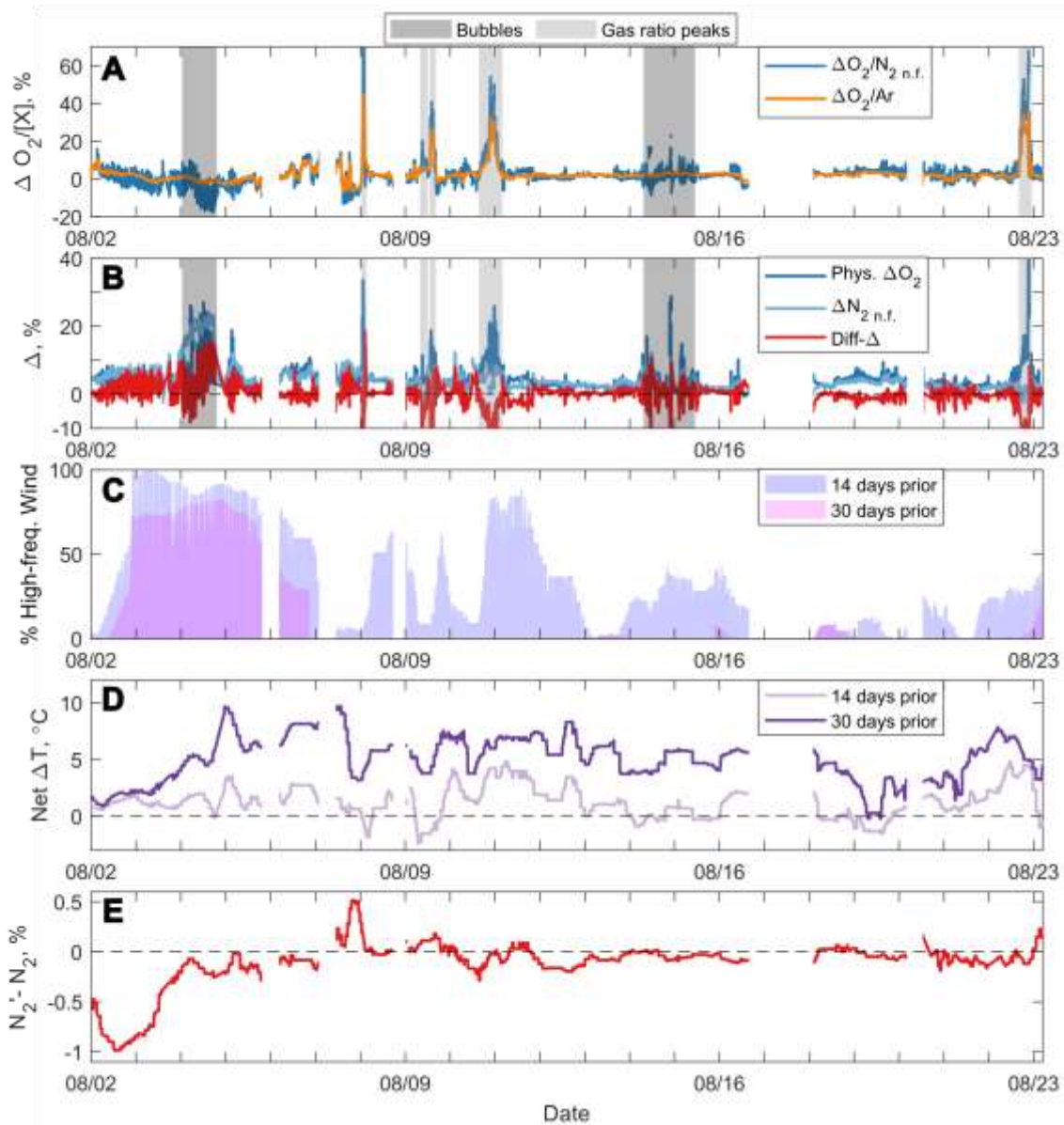
Figure 3: (A) Time-series of $\Delta O_2/Ar$ and noise-filtered (n.f.) $\Delta O_2/N_2$, where shaded areas indicate either noise due to bubbles in the underway seawater line or large gradients in gas ratios as determined by observation. The $\Delta O_2/N_2$ peak off the chart is at 119%. (B) Time-series of Diff-Δ, ΔO_2-physical, and noise-filtered ΔN_2, where artifacts of the data due to mismatched gas ratio peaks (Diff-Δ shaded in light gray) are off the chart and should not be considered. (C) Percent of 3-hourly average wind speed measurements exceeding 10 m s^{-1} over 14 and 30 days prior to sampling where collocated with cruise track. (D) Net temperature change over 14 and 30 days prior to sampling, collocated with cruise track, based on satellite SST reanalysis. (E) Difference between N_2' and N_2 along the cruise track.

22

431 oxygen supersaturation, the ratios were observed to differ, where $\Delta O_2/N_2$ was consistently

432 greater than $\Delta O_2/Ar$ (Figure 3A). The memory effects associated with the EIMS effectively slow

433 down the $\Delta O_2/Ar$ measurements, resulting in $\Delta O_2/Ar$ that did not reach the true maximum value

434 during sharp gradients, while $\Delta O_2/N_2$ is likely capturing these maxima more accurately due to

435 the faster response time. This is supported by discrete O_2/Ar bottle samples, which were greater

436 than corresponding EIMS O_2/Ar measurements by about 5% during two steep gradients on this

437 cruise, corroborating the idea that the EIMS is not measuring the true value during these peaks in

438 net biological oxygen production.

439   The median of diff-Δ over the cruise was 0.53%, indicating that $\Delta O_2/Ar$ was generally

440 greater than $\Delta O_2/N_2$, while there were many large excursions from these values (Figure 3B). In

441 particular, deviations in diff-Δ occurred during time periods where strong gradients in oxygen

442 were encountered and in areas with overwhelming bubble influence (shaded regions, Figure 3B).

443 The spread of diff-Δ remains similar when observing all diff-Δ values compared to baseline

444 values (which excludes data associated with steep gas peaks and data with substantial bubble

445 noise, Figure 4), with a roughly normal

446 distribution of diff-Δ where 90% of

447 baseline observations were between -2.2%

448 and 3.5%.

449   While the median value of diff-Δ

450 was small overall (0.53%) and is

451 comparable to the uncertainty in O_2/N_2 (as

452 discussed in section 3.6), it is still useful to
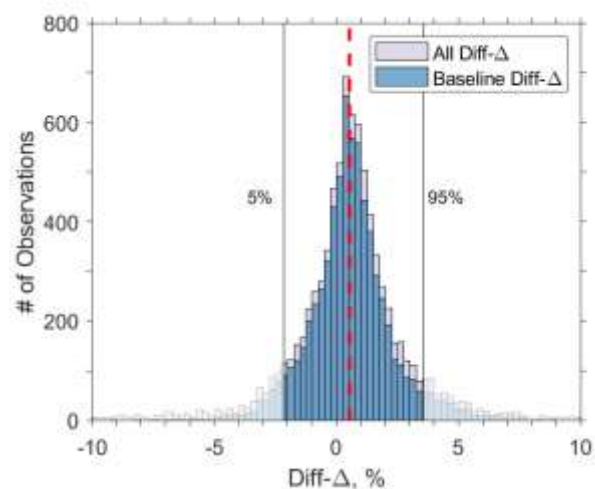
453 understand potential biases that may

Figure 4: Histogram of diff-Δ observations with all values and with baseline values (when erroneous data due to bubbles and steep gas peaks are excluded).

23

454 contribute to differences between O_2/Ar and O_2/N_2 for this data. A potential source of bias in

455 ΔO_2/N_2 and thus diff-Δ may arise from the assumed saturation of less prevalent gases,

456 particularly Ar. On this cruise, Ar concentrations were determined by EIMS O_2/Ar ratio and

457 optode oxygen measurements (where $[Ar]=[O_2]_{optode}/[O_2/Ar]_{EIMS}$), yet these values were not used

458 in calculations of ΔO_2/N_2, as this study is intended to simulate the comparability of these

459 methods, and the inclusion of calculated Ar values is not anticipated to be available with most

460 GTD deployments. If these calculated values for Ar were included, which indicate Ar was

461 consistently supersaturated throughout this

462 cruise, the bias in diff-Δ does not change

463 considerably, with a median of 0.48%. We

464 investigate other potential sources of bias

465 from physical forcing in section 3.3.

466 *3.3.   Evaluating physically-driven bias in*

467 *O_2/N_2 relative to O_2/Ar*

468   Differences in ΔO_2/Ar and ΔO_2/N_2,

469 i.e., diff-Δ, are expected due to a variety of

470 physical factors including gas solubility,

471 bubble injection, and gas exclusion

472 principles. For example, an increase in

473 temperature instantaneously changes the gas

474 solubility in the water mass; the solubility of

475 Ar and O_2 will change similarly due to their

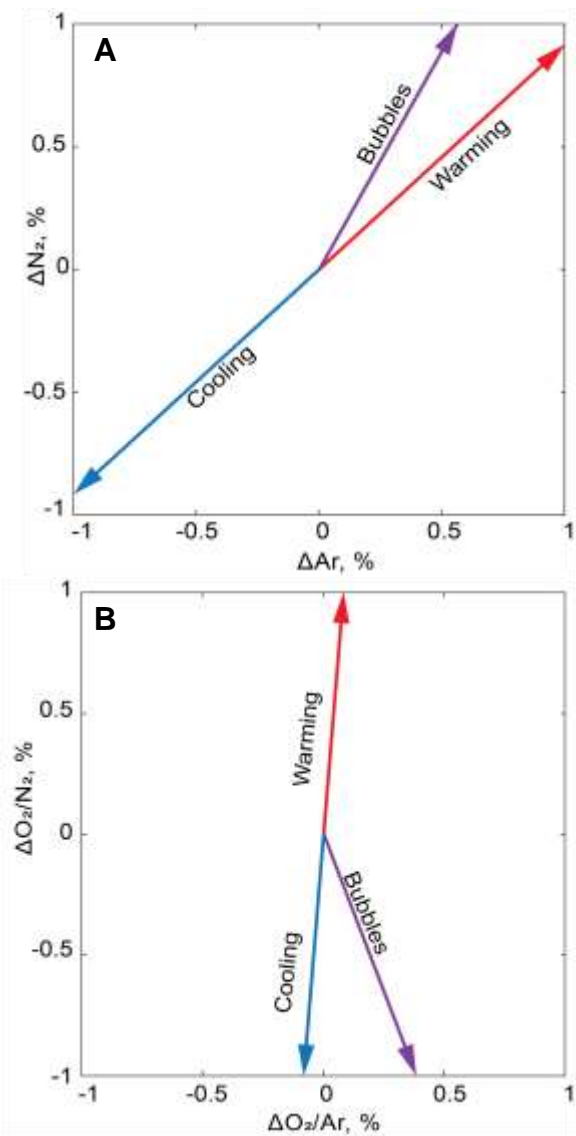476 comparable solubility, while N_2 solubility

Figure 5: Expected changes in ΔAr, ΔN_2, ΔO_2/Ar and ΔO_2/N_2 due to temperature change and bubble injection.

24

477　decreases to a lesser extent because it is less soluble. This difference in temperature effect

478　between N_2 and Ar appears small in the individual gas saturation anomalies (Figure 5A) but

479　becomes amplified when calculating gas ratios due to the dissimilarity between N_2 and O_2. The

480　result is an $\Delta O_2/N_2$ ratio change in response to temperature that is 12 times greater than $\Delta O_2/Ar$

481　(Figure 5B). For example, warming of 5°C would result in relatively similar increases in O_2, N_2,

482　and Ar saturations (11.3%, 10.4%, and 11.2% respectively) but pronounced differences between

483　the $\Delta O_2/Ar$ and $\Delta O_2/N_2$ gas ratios (0.18% and 0.83% respectively). The resulting change in diff-

484　Δ ($\Delta O_2/Ar$ - $\Delta O_2/N_2$) would be -0.65%.

485　This warming-induced saturation signal

486　will erode via exchange with the

487　atmosphere over subsequent weeks as the

488　upper ocean re-equilibrates to the new

489　temperature (Figure 6A).

490　　　　Conversely, wind-driven bubble

491　injection creates a gas supersaturation due

492　to enhanced gas injection which increases

493　over the period of enhanced wind. Bubble

494　injection and bubble exchange,

495　parameterized as wind-driven based on the

496　equations of Woolf and Thorpe (1991),

497　will increase individual gas saturations but

498　will decrease the $\Delta O_2/N_2$ ratio due to the
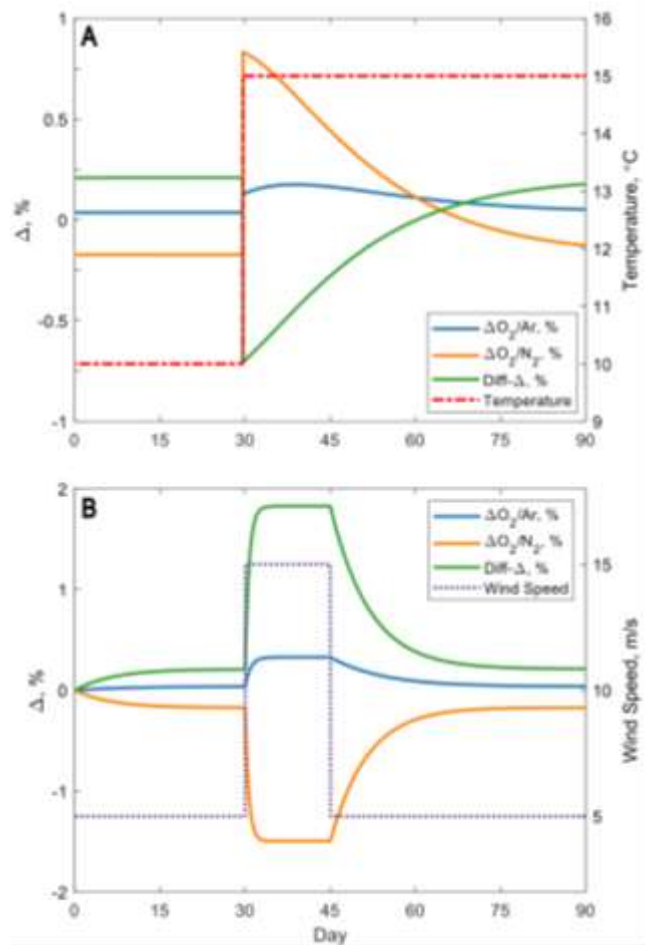
499　high mole fraction of N_2 in the atmosphere

Figure 6: Box model of gas saturation change in $\Delta O_2/Ar$ and $\Delta O_2/N_2$ with (A) warming water and (B) increased wind speed. Baseline parameters include a mixed layer depth of 20 meters, temperature of 10°C, salinity of 32 and wind speed of 5 m/s.

25

500   and the relatively low solubility of N_2 in seawater. The wind-driven supersaturation of N_2 is

501   much larger than the supersaturation of more soluble gases (O_2, Ar), such that enhanced wind

502   will increase diff-Δ. If wind speed increases from 5 m/s to 15 m/s and remains at 15 m/s, the

503   resulting equilibrium diff-Δ will reach a maximum of 1.8%, where diff-Δ will equal 95% of the

504   maximum (1.8%) in 2 days based on the estimated effect of bubbles injected into the surface

505   ocean and the solubility differences between N_2 and Ar (Figure 6B). The expected change in gas

506   saturation and gas ratio saturation from temperature change and enhanced wind are indicated in

507   Figure 6 where the relaxation back to equilibrium (defined as within 10% of the equilibrium

508   value) following either a high wind event or temperature change is slow (~6-8 weeks).

509   Because O_2/N_2 is likely to be more sensitive to physical forcing than O_2/Ar, one way of

510   assessing causes of observed diff-Δ and hence biases in O_2/N_2 is by comparing diff-Δ values to

511   an approximation of physical forcing, estimated as:

512    $\Delta O_2^{phys} = \Delta O_2^{total} - \Delta O_2/Ar$ (11)

513   where the last term ($\Delta O_2/Ar$) represents ΔO_2^{bio} (Shadwick et al. 2015). When ΔO_2^{phys} is positive,

514   a positive physical supersaturation of oxygen is estimated and could be indicative of recent

515   warming of the water mass or potential influence of bubbles. Along the same lines, a negative

516   value is expected when biological oxygen saturation is greater than total oxygen saturation,

517   potentially caused by recent cooling. The estimate of ΔO_2^{phys} over this cruise has a mean value of

518   3.7% (Figure 3B). This ΔO_2^{phys} estimate may indicate that the small difference between O_2/Ar

519   and O_2/N_2 is due to recent wind-forcing on the water mass; this is because of a combination of

520   the physical oxygen supersaturation and median positive diff-Δ, where positive diff-Δ results

521   from bubbles or cooling (and negative diff-Δ results from warming). Physical forcing estimates

522   from this cruise (Figure 3C and 3D) did not appear to be directly related to observed diff-Δ over

26

523   the span of this cruise, yet a more accurate approach of modeling water mass history could better

524   approximate the solubility-based differences between O_2/Ar and O_2/N_2.

525   Recently, Izett and Tortell (2020b) introduced a calculated value, N_2', that corrects for solubility

526   differences between N_2 and Ar using historical water mass data, where N_2' is an approximation

527   of Ar, a physical analog to O_2 (Izett and Tortell 2020b; Izett et al. 2021). If N_2' and N_2 differ

528   significantly, a large component of physical bias exists in O_2/N_2 due to physical forcing and

529   reequilibration dynamics, but O_2/N_2' could be calculated to adjust for the expected solubility

530   differences due to the historical physical forcing. Our estimated N_2' is similar to measured N_2 for
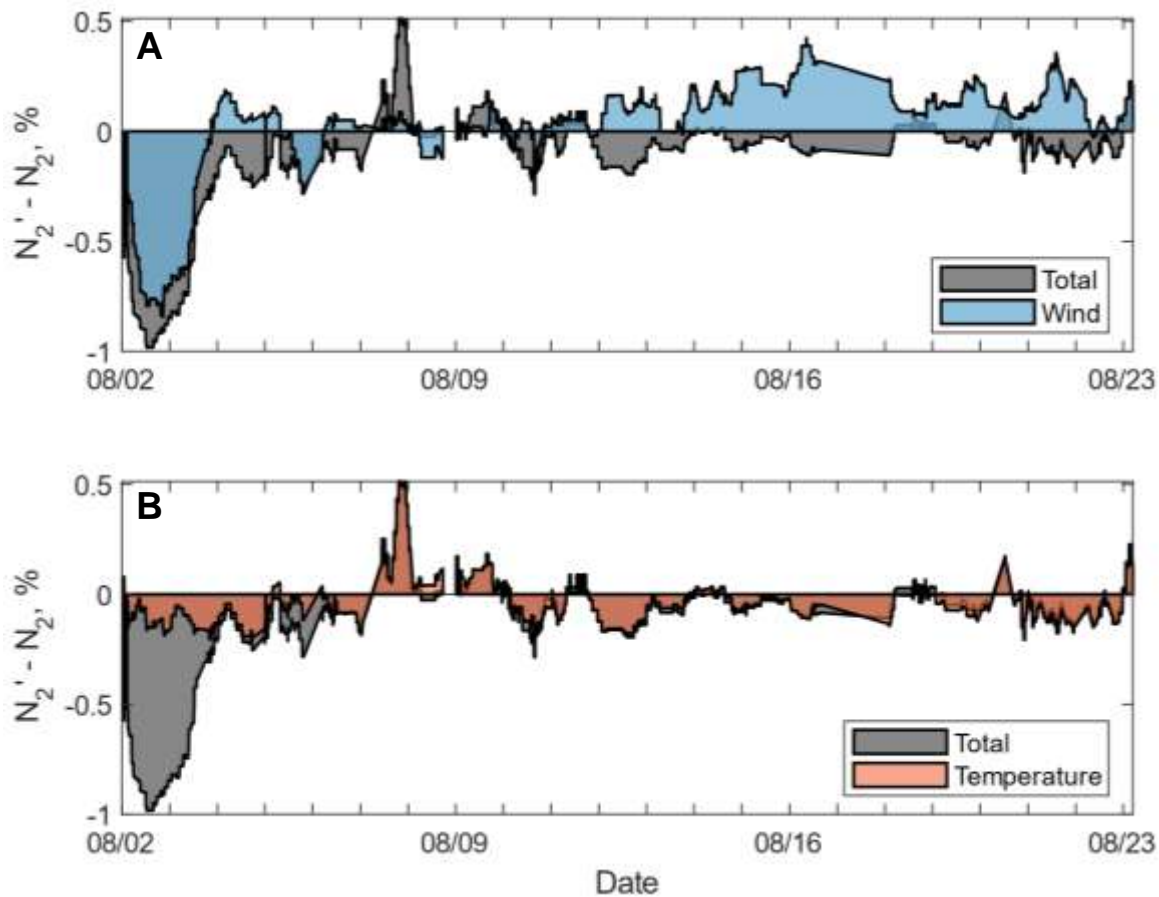

Figure 7: (A) Modeled $N_2' - N_2$ compared to the wind component, $N_2'_{wind} - N_2$. $N_2'_{wind}$ is estimated by taking the difference between N_2' and N_2' when historical wind speed is set constant, equal to wind speed at cruise occupation. Areas where these align indicate that historical wind speed is the main driver of saturation differences. (B) Modeled $N_2' - N_2$ compared to the temperature component, $N_2'_{temp} - N_2$. $N_2'_{temp}$ is estimated by taking the difference between N_2' and N_2' when historical sea surface temperature is set constant, equal to temperature at cruise occupation. Areas where these are similar indicate that past temperature change is the main driver of saturation differences.

27

531   most of this cruise (Figure 3E), with deviations that may be attributed to wind and temperature

532   change (Figure 7).

533   Over the first two days of the cruise in the southern Bering Sea, wind was the

534   predominant driver of the negative difference between N_2' and N_2, which was also the case

535   intermittently over the following few days (Figure 7A). This was determined based on both the

536   relatively high-frequency winds, small temperature change (Figure 3), and the results of a pair of

537   N_2' modeling calculations in which either historical temperature or wind speed was held constant

538   at values measured on the cruise (Figure 7). After the initial wind-dominated days in the Bering

539   Sea, the combination of wind and warming temperatures resulted in near-zero difference in N_2'

540   and N_2, where the two factors likely balanced each other out at times. The estimates of N_2'

541   contributions do not combine to equal the calculated difference in N_2' and N_2, as assumptions

542   were made about the constant temperature or wind speed that contribute to erroneous estimates,

543   yet they are a rough approximation of the role each factor plays in the correction of solubility

544   differences.

545   The difference in N_2' and N_2 throughout the cruise was not directly correlated to the

546   estimates of physical forcing described here (high-frequency wind, average wind speed, and net

547   temperature change over 14 and 30 days, Figure 3). This is suspected to be in part due to the

548   cumulative nature of physical forcing by temperature change and wind, inaccuracies in satellite-

549   based wind speeds, and the averaging that was used in these estimates, where wind and

550   temperature changes in the day or two prior to measurement will be more strongly reflected in

551   N_2' than those two weeks prior. Additionally, the calculations of N_2' performed here excluded

552   vertical mixing due to lack of gas saturation data at depth, yet complete absence of vertical

553   mixing is unlikely and therefore contributes to uncertainty in estimated N_2'.

28

554   The small overall differences in N_2' and N_2 throughout most of this cruise were

555   consistent with findings by Izett et al. (2021) of minimal difference in these tracers in the

556   Canadian Arctic Archipelago and Baffin Bay. This suggests that application of the O_2/N_2

557   approach could be promising in the Pacific Arctic region, but further evaluation under a range of

558   physical conditions is still needed. The use of O_2/N_2' could improve the utility of the GTD

559   method, yet the advective nature of water masses should be accounted for in a study area, where

560   highly advective regions may be inaccurately modeled by georeferenced data prior to sampling.

561   In this study region, where advection of water masses can be relatively rapid, the reconstructed

562   water mass history used in calculating N_2' could be erroneous at times.

563   *3.4.   Sea ice and biological influences on dissolved O_2, N_2, and Ar*

564   Other factors that influence gas saturation include sea ice formation, sea ice melt, and

565   biologically-driven N_2 fixation or denitrification. For this dataset, we expect these processes to

566   contribute insignificantly toward driving differences between O_2/N_2 and O_2/Ar. During sea ice

567   formation, brine rejected from the ice matrix is expected to be enriched in Ar, O_2, and N_2 due to

568   the exclusion of larger gas molecules during the freezing process. This brine sinks to depth,

569   enriching deep water in these gases. When vertical mixing of these deep waters occurs, a brine

570   signal may be observed in the resulting water, which is expected to be enriched in Ar compared

571   to N_2 based on gas partitioning between bubbles, ice, brine, and residual water (Hood 1998;

572   Hood et al. 1998). In contrast, the meltwater signal is expected to be depleted in larger gases (Ar,

573   O_2, N_2) due to gas exclusion during sea ice formation. This meltwater effect is not anticipated to

574   be represented in this dataset due to lack of sea ice during and directly prior to this cruise, but

575   brine signatures could be observed in areas where vertical mixing brings waters that have been

576   seasonally isolated at depth to the surface.

29

577   Biological influences on dissolved N_2 in the ocean, including nitrogen fixation and

578   denitrification, typically have a small overall effect on the dissolved N_2 saturation anomaly

579   (ΔN_2). The effect of nitrogen fixation, calculated based on the maximum rate of nitrogen fixation

580   estimated by Shiozaki (2018) in the Chukchi Sea, is negligible on ΔN_2 (<0.01%). The effect of

581   denitrification on the shallow Bering and Chukchi shelves has a potentially greater effect on N_2.

582   Vertical mixing of deep water containing biologically elevated dissolved N_2 will influence the

583   O_2/N_2 ratios measured at the surface, resulting in lower-than-expected $\Delta O_2/N_2$. With seasonal

584   dissolved inorganic nutrient deficits (3.9 µM N) at depth on the Chukchi shelf (Mordy et al.

585   2021), vertical mixing of 20% of the water column would result in a 0.06% decrease in $\Delta O_2/N_2$

586   in the surface mixed layer, a small and likely indiscernible bias. Since the Chukchi Sea is

587   seasonally well-stratified, more significant vertical mixing of the water column is only likely to

588   occur near coastal features or areas with enhanced mixing, such as near Bering Strait.

589   *3.5.   Net Community Production*

590   The median NCP estimated by O_2/Ar and O_2/N_2 was 9.3 ± 2.8 and 7.9 ± 3.2 mmol O_2 m^{-2}

591   day^{-1}, respectively, for all

592   regions with comparable

593   data (which excludes bubble-

594   impacted areas, as well as

595   one region in Chirikov Basin

596   with a clear vertical mixing

597   signal). The overall NCP

598   estimated by O_2/Ar and $O-$
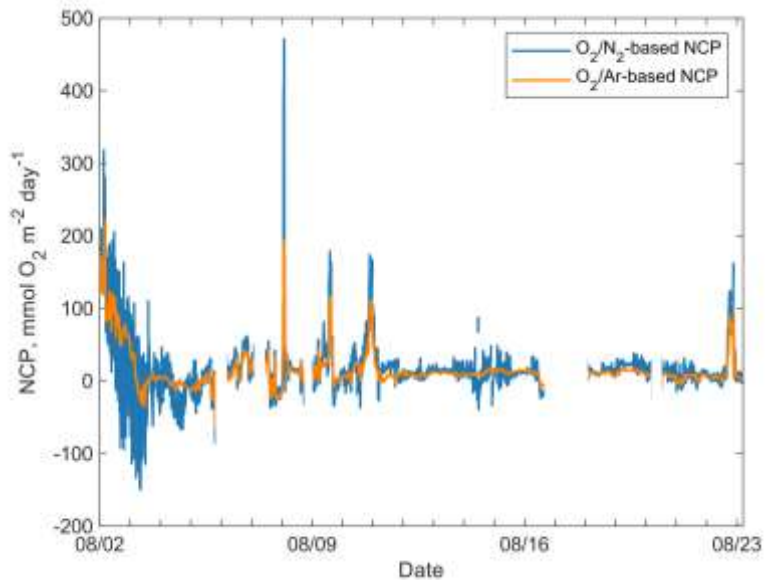
599    $_2/N_2$ are similar, with slightly

Figure 8: NCP calculated based on O_2/Ar and residual filtered O_2/N_2 for measurements within the bounds described.

30

600   larger values based on O_2/N_2, while differences include the discrepancy in maximum NCP in

601   regions with large gradients as previously discussed, as well as increased noise in O_2/N_2 signal

602   (Figure 8).

603   The median NCP based on O_2/Ar measurements was 9.8 mmol O_2 m^{-2} day^{-1}, while 95%

604   of the values fell between -18 and 100 mmol O_2 m^{-2} day^{-1}. Assuming NCP is primarily new

605   production fueled by nitrate, we use an O_2:C ratio of 1.4 (Laws 1991), where O_2/Ar-based NCP

606   ranged from below zero to >1000 mg C m^{-2} day^{-1}, with a median of 84 mg C m^{-2} day^{-1} during this

607   August cruise. Since this measurement technique integrates over the preceding weeks, this

608   unique dataset may better capture episodic events that are missed by shorter-term incubations.

609   These measurements therefore fill an important temporal gap between short-term incubations

610   and large-scale seasonal drawdown estimates calculated at the regional scale. By utilizing O_2/N_2-

611   based NCP estimates in remote regions including the subpolar and polar seas, variability due to

612   seasonal patterns and episodic events contributing to NCP could be more completely understood.

613   Given that these NCP estimates fill a unique temporal gap it is useful to compare to prior

614   estimates. Seasonal NCP estimates based on DIC and nutrient drawdown (Mathis et al. 2009;

615   Codispoti et al. 2013) in the Chukchi Sea include the spring bloom, and are therefore expected to

616   be considerably higher than our rates measured in August, post-bloom. Annual measurements

617   (Mordy et al. 2020) include the dark, ice-covered winter when production is absent and may be

618   more in line with our post-bloom estimates. Generally, these patterns are what we see when we

619   compare to prior estimates (Table 1). However, it is important to note that interannual variability

620   in this region is large, and the Chukchi and Bering Seas were noted to have particularly high sea

621   surface temperatures in 2019, which may have led to an uncharacteristic environment (Andersen

622   et al. 2020).

623   With the spatially resolved data from this cruise, patterns of surface productivity can be

624   assessed, and potential drivers of biological production can be explored. Areas of high NCP from

625   this cruise were consistent with previously observed biological hotspots in the Chirikov Basin

626   and off of Point Hope (Distributed Biological Observatory regions 2 and 3, respectively,

627   Grebmeier et al. 2010). More broadly, the observations illustrate that NCP is spatially patchy, as

Table 1: NCP comparisons in Chukchi Sea

Method	NCP (mg C m^{-2} day^{-1})	Region	Timescale	Source
DIC Drawdown	8 to >2000 (range of values)	Northeast Chukchi Sea	Seasonal, spring to summer	Mathis et al. 2009
Nutrient drawdown	1167	Southern Chukchi Sea	60-day growing period	Codispoti et al. 2013
Seasonal nitrate	82 to 192	Eastern Chukchi Sea	Annual, between 2010-2018	Mordy et al. 2020
Shipboard O_2/Ar	8 to 86 [1 to 10 mmol O_2 m^{-2} day^{-1}]	Chukchi Sea	Integrated over few weeks in October 2011 and 2012	Juranek et al. 2019
Shipboard O_2/Ar	84 [9.8 mmol O_2 m^{-2} day^{-1}]	Chukchi Sea	Integrated over few weeks in August 2019	this study

628   has been previously noted (Juranek et al. 2019). These patterns may be missed by traditional

629   incubation sampling approaches. Patchy regions of high NCP on this cruise may be a result of

630   nutrient input through the convergence of water masses, which was noted in Chirikov Basin

631   where Anadyr water was present, as well as near Pt. Hope due to the combination of upstream

632   mixing in Bering Strait and water flow around the headland of Pt. Hope (Figure 9). In the

633   Chirikov Basin, NCP calculations were determined to not meet steady state requirements, since

634   these areas were subject to significant mixing as noted by CTD casts with uniform temperature

635   and salinity profiles. In the Pt. Hope region, the high NCP observed by gas ratio methods, which

636   at times contrasted with the measured chlorophyll, was indicative of the intermittent nature of

637   blooms in this region. These variations are due to the coexistence of favorable light and nutrient

638   conditions, which can vary due to changes in water masses, mixed layer depth, and/or wind
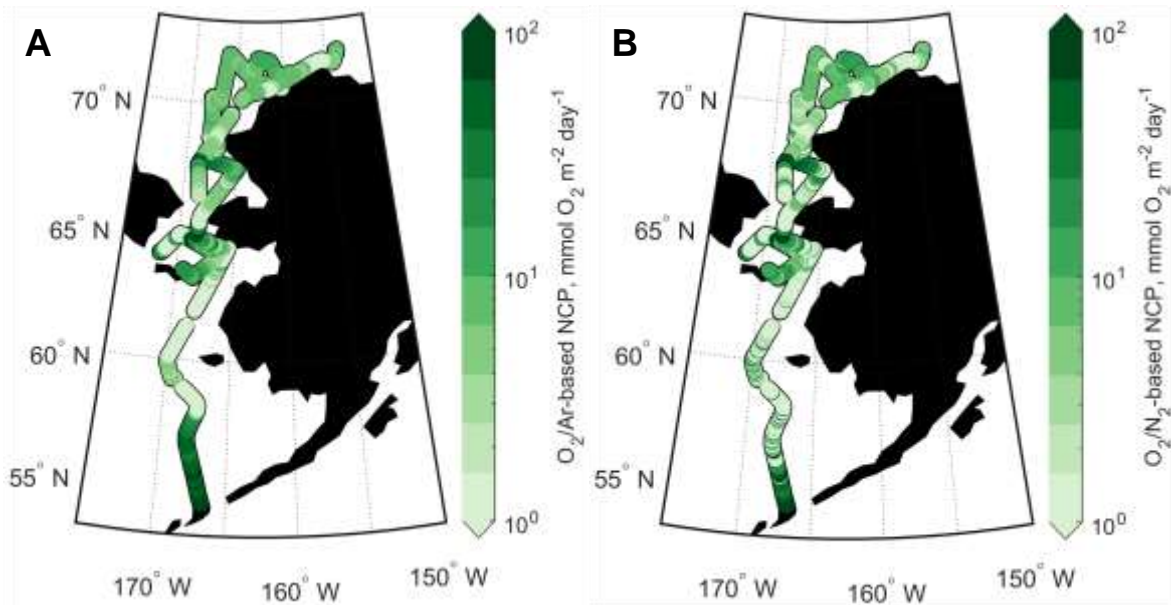
639   patterns.

Figure 9 : (A) O_2/Ar-based NCP and (B) O_2/N_2-based NCP along the cruise track (scale attenuated, where range is -64 to 224 and -184 to 491, respectively).

33

640   In the southern Bering Sea, NCP was elevated near the Aleutian Islands and near Bering

641   Strait, while lower values were estimated in the eastern central Bering Sea where high winds

642   were observed. The southern Bering Sea had some of the highest NCP measurements with a

643   bimodal distribution where the majority of NCP estimates were near equilibrium and a smaller

644   grouping of values between 50 and 100 mmol O_2 m^{-2} day^{-1}. The northern Bering Sea also had a

645   large proportion of NCP estimates near equilibrium, with some elevated values primarily around

646   Chirikov Basin and Bering Strait. The most dynamic region observed on this cruise was the

647   southern Chukchi sea, where NCP was generally positive with an average of 24 mmol O_2 m^{-2}

648   day^{-1}, while this was also the region where hotspots were observed near Pt. Hope. The northern

649   Chukchi and Beaufort seas had relatively consistent NCP that was representative of the median

650   NCP throughout the cruise of near 10 mmol O_2 m^{-2} day^{-1}, with limited variance in these areas.

651   By observing the seasonal patterns in NCP in high resolution, connections to wind

652   events and water mass convergences could be better understood, ultimately providing a better

653   foundation for deciphering future patterns of productivity within this dynamic environment. As

654   this cruise took place in an unusually warm year with early ice retreat, these observations from

655   August 2019 may deviate from patterns observed in colder years.

656   *3.6.   Uncertainty analysis*

657   To estimate uncertainty in EIMS- and GTD-based NCP, we used a Monte Carlo approach

658   that involves randomly varying the estimated error of each parameter involved in calculating

659   NCP, assuming a normal distribution of error. The values used in these determinations are found

660   in Table 1, where uncertainty was calculated based on 1000 determinations of $\Delta O_2/Ar$- and

661    $\Delta O_2/N_2$-based NCP with Equation 10 for gas ratios observed on this cruise. Absolute uncertainty

662   in the measurement of O_2/Ar of $\pm 0.25\%$ was determined by the standard deviation of O_2/Ar in

34

663   air standards (n=27) measured by IRMS, since EIMS O_2/Ar measurements were corrected to the

664   calibration bottle samples analyzed by IRMS. For GTD-based measurements, an absolute

665   precision in the measurement and calculation of O_2/N_2 of ±0.57% was determined by

666   propagation of error in Equations 6 and 7 (Table 2). Izett et al. (2021) estimated the uncertainty

667   in $\Delta O_2/N_2$ at 1.3%, which also included uncertainties for warming-induced supersaturation in the

668   underway ship lines, calibration of O_2/N_2, and the assumptions in constraining Ar. This error

669   analysis may better

670   approximate the

671   uncertainties in $\Delta O_2/N_2$, yet the effect of

672   this random

Table 2: Error estimates used in Monte Carlo approach of uncertainty and output uncertainty in $\Delta O_2/Ar$ and $\Delta O_2/N_2$.

Source	Estimated Error		
O_2/Ar_{meas}	0.25% (St. Dev. Of O_2/Ar in air)		
O_{2sol}	0.3% (Garcia and Gordon 1992)		
Gas exchange, k	20% (Wanninkhof 2014)		
GTD total pressure	0.2% or 2 mbar (Pro-Oceanus TDGP manual)		
O_2 (Winkler-corrected optode)	0.5% or 1.1 mbar (McNeil et al. 2005)		
Atmospheric pressure (NCEP reanalysis)	0.5% or 5 mbar (Padin et al. 2007)		
Uncertainty			
	Absolute	Relative error, $\Delta O_2/[X]$ = 1% or 10%	
O_2/Ar	0.25%	1 ± 0.41 %	10 ± 0.42 %
O_2/N_2	0.57%	1 ± 0.66 %	10 ± 0.75 %

673   this random

674   uncertainty on NCP

675   estimates is very

676   small due to the far

677   greater uncertainty in

678   constraining the gas

679   transfer term.

680   Uncertainty in the gas transfer coefficient, k_{O2} (± 20%) (Wanninkhof 2014), makes up the

681   largest component of uncertainty in NCP. The resulting uncertainty for a simulated NCP of 10

682   mmol O_2 per m^2-day from O_2/Ar and O_2/N_2 is 30% and 36%, respectively, with a proportionally

683   lower error with larger NCP rate. The uncertainty in O_2/Ar-based NCP ranged from 16% to

684   >100%, while the uncertainty for O_2/N_2-based NCP ranged from 20% to >100%. Importantly,

685   while uncertainty in $\Delta O_2/N_2$ becomes large in areas where net biological oxygen supersaturation

35

686   nears zero, these estimates still discern the relative magnitude and direction of NCP for the

687   majority of observations on this cruise, so long as the oxygen measurements used to compute

688   O_2/N_2 are well-calibrated.

689   The uncertainty outlined above is based on the accuracy in the measurement and

690   calculation of $\Delta O_2/N_2$, and does not include potential biases from physical forcing that cause this

691   tracer to inaccurately track ΔO_{2bio} (see Section 3.3). When comparing median diff-Δ (0.53%) to

692   the methodological uncertainty of 0.57% in $\Delta O_2/N_2$, the bias represented by diff-Δ is of similar

693   magnitude. The distribution of baseline diff-Δ, between -2.2% and 3.5% for 90% of

694   observations, is attributed to the cumulative saturation effects of both bubbles and temperature

695   change, while potential variations in Ar saturation could have also played a small role. Bubbles

696   were the primary driver in the southern Bering Sea, while temperature change was likely more

697   important in the Chukchi Sea, as inferred from the modeling described above.

698   *3.7.   Strengths and weaknesses of GTD and EIMS approaches*

699   A potential limitation of gas ratio estimates from a GTD is the dependence on accurate

700   oxygen measurements when calculating O_2/N_2. This requires optode calibration to adjust for

701   offsets and drift, where a 5% inaccuracy in measured optode O_2 (the average offset on this

702   cruise), would result in a difference of 6.5% in O_2/N_2. Without reliable oxygen calibrations, this

703   scale of difference could result in ambiguous NCP estimates derived from O_2/N_2, although areas

704   with strong biological signals are still qualitatively identified despite this potential uncertainty.

705   This is expected to be a greater issue when frequent O_2 calibration samples are not feasible, e.g.

706   with autonomous deployments, although periodic air calibration of deployed oxygen sensors

707   could serve as an alternative calibration method (Bittig and Körtzinger 2015; Bushinsky et al.

708   2016).

36

709   A challenge experienced with the GTD-optode system on this cruise was the effect of

710   bubbles in the surface ocean. Bubble effects are likely to be a problem for ships with shallow

711   seawater intakes (<5 m) operating in moderate to rough sea states. While a debubbling chamber

712   could be employed to limit this noise, areas with extensive bubble influence in the GTD/optode

713   data are expected to be influenced by bubble injection and exchange in the water column as well,

714   which would still bias the measured O_2/N_2.

715   This method comparison revealed a smoothing of oxygen peaks in the EIMS data, which

716   we attribute to the EIMS equilibrator memory effect. Optode O_2 and GTD-based O_2/N_2 peaks

717   were much sharper and reached higher maximum values in biological hotspots; in these areas,

718   the observed O_2/N_2 was up to 1.5 times greater than O_2/Ar. Therefore, in regions with sharp

719   gradients and localized productivity peaks, such as those encountered in this study in the

720   Chirikov basin and the vicinity of Pt. Hope, GTD measurements may more accurately capture

721   absolute productivity values, while EIMS-based observations provide better accuracy in

722   oligotrophic, lower-productivity regions that characterized the rest of the cruise track. On future

723   deployments, EIMS equilibrator response times could also be better optimized by using an

724   equilibrator cartridge with a smaller headspace to water volume ratio, while including a

725   recirculating desiccant loop for constant removal of water vapor in the equilibrator has also been

726   shown to improve response time (Manning et al. 2016).

727   **4.   Conclusions**

728   This cruise provided a range of conditions under which to assess the efficacy of the

729   GTD/optode system compared to the EIMS for estimating net biological oxygen production. An

730   important takeaway from this method comparison is the relatively quick response time of the

731   GTD, which allows sharp gradients in gas saturation that generally characterize biological

37

732   hotspots to be well characterized. This method is subject to greater biases from temperature

733   change and bubble injection than the more commonly used O_2/Ar approach. However, we found

734   these biases to be generally small in the Bering and Chukchi Sea during the OS1901 cruise,

735   suggesting the GTD/optode approach may be useful for expanding seasonal observations of

736   productivity in this region. Using historical modeling to approximate O_2/N_2' (Izett and Tortell

737   2021) or utilizing time series measurements on a mooring or drifter that could record the

738   physical changes over time in a given water mass, the expected divergence of ΔO_2/N_2 from

739   ΔO_2/Ar can be estimated.

740   The utility of the GTD/O_2 method depends on the productivity in an area: it is expected to

741   capture large signals in net biological oxygen supersaturation, while oligotrophic areas with low

742   net productivity may be more difficult to determine with certainty. If physical factors influencing

743   solubility are decomposed and accounted for, as Izett and Tortell (2021) do with O_2/N_2', the

744   near-equilibrium ΔO_2/N_2 can still be used as an estimate of biological oxygen, with some

745   inherent uncertainty. In this study, ΔO_2/N_2 was typically less than ΔO_2/Ar, which means it likely

746   results in NCP estimates that are slightly underestimated throughout most of the cruise. In

747   regions with very low production, the use of ΔO_2/N_2 could result in occasional instances when an

748   NCP estimate is negative (NCP<0) where ΔO_2/Ar indicates net autotrophy .

749   The dependence of ΔO_2/N_2 on calibrated oxygen measurements also needs to be

750   considered when using the GTD/optode method in an autonomous deployment. By incorporating

751   periodic air measurements by the optode, a strategy that has previously been used on floats

752   (Bittig and Körtzinger 2015), reliable oxygen measurements could be maintained throughout a

753   GTD/optode deployment, providing a reference for calibration.

38

754   The median value of mixed layer integrated NCP was 9.3 ± 2.8 and 7.9 ± 3.2 mmol O_2 m$^-$

755   ^{2} day^{-1}, based on O_2/Ar and O_2/N_2, respectively. The range of NCP was large, from less than zero

756   to >100 mmol O_2 m^{-2} day^{-1}, with some of the largest NCP estimates measured at well-established

757   hotspots in the Pacific Arctic. The spatial patterns of NCP indicate areas where enhanced mixing

758   may stimulate biological productivity on an intermittent basis, patterns that are difficult to map

759   and monitor with shorter-term incubation-based approaches. Our observations indicate that the

760   GTD/optode method provides promising potential for autonomous observations in the future,

761   which will allow for improved understanding of NCP and the mechanisms driving this

762   production in dynamic environments such as the Pacific Arctic.

763   **Acknowledgements**

776 Laboratory and contribution No. 1146 for CICOES and contribution No. 1011 for NOAA's

777 Ecosystem Fisheries Oceanography Coordinated Investigations.

778 **References**

779 Andersen, J. K., L. M. Andreassen, E. H. Baker, and others. 2020. State of the Climate in 2019:

780   The Arctic J. Richter-Menge and M.L. Druckenmiller [eds.]. Bull. Am. Meteorol. Soc. **101**:

781   S239–S286. doi:10.1175/BAMS-D-20-0086.1

782 Anderson, L. G., and S. Kaltin. 2001. Carbon fluxes in the Arctic Ocean—potential impact by

783   climate change. Polar Res. **20**: 225–232. doi:10.3402/polar.v20i2.6521

784 Arrigo, K. R., and G. L. van Dijken. 2015. Continued increases in Arctic Ocean primary

785   production. Prog. Oceanogr. **136**: 60–70. doi:10.1016/j.pocean.2015.05.002

786 Arrigo, K. R., G. van Dijken, and S. Pabi. 2008. Impact of a shrinking Arctic ice cover on marine

787   primary production. Geophys. Res. Lett. **35**: 1–6. doi:10.1029/2008GL035028

788 Baker, M. R., E. V. Farley, S. L. Danielson, C. W. Mordy, K. M. Stafford, and D. M. S. Dickson.

789   2022. Integrated Research in the Arctic – ecosystem linkages and shifts in the northern

790   Bering Sea and eastern and western Chukchi Sea. Deep. Res. II.

791 Baker, M. R., E. V. Farley, C. Ladd, S. L. Danielson, K. M. Stafford, H. P. Huntington, and D.

792   M. S. Dickson. 2020. Integrated ecosystem research in the Pacific Arctic – understanding

793   ecosystem processes, timing and change. Deep. Res. Part II Top. Stud. Oceanogr. **177**.

794   doi:10.1016/j.dsr2.2020.104850

795 Bélanger, S., M. Babin, and J.-É. Tremblay. 2013. Increasing cloudiness in Arctic damps the

796   increase in phytoplankton primary production due to sea ice receding. Biogeosciences **10**:

797   4087–4101. doi:10.5194/bg-10-4087-2013

40

798   Benson, B. B., and D. Krause. 1984. The concentration and isotopic fractionation of oxygen

799   dissolved in freshwater and seawater in equilibrium with the atmosphere1. Limnol.

800   Oceanogr. **29**: 620–632. doi:10.4319/lo.1984.29.3.0620

801   Bittig, H. C., and A. Körtzinger. 2015. Tackling oxygen optode drift: Near-surface and in-air

802   oxygen optode measurements on a float provide an accurate in situ reference. J. Atmos.

803   Ocean. Technol. **32**: 1536–1543. doi:10.1175/JTECH-D-14-00162.1

804   Bushinsky, S. M., S. R. Emerson, S. C. Riser, and D. D. Swift. 2016. Accurate oxygen

805   measurements on modified argo floats using in situ air calibrations. Limnol. Oceanogr.

806   Methods **14**: 491–505. doi:10.1002/lom3.10107

807   Carmack, E. C., and P. Wassmann. 2006. Food webs and physical–biological coupling on pan-

808   Arctic shelves: Unifying concepts and comprehensive perspectives. Prog. Oceanogr. **71**:

809   446–477. doi:10.1016/j.pocean.2006.10.004

810   Carmack, E., I. Polyakov, L. Padman, and others. 2015. Toward quantifying the increasing role

811   of oceanic heat in sea ice loss in the new arctic. Bull. Am. Meteorol. Soc. **96**: 2079–2105.

812   doi:10.1175/BAMS-D-13-00177.1

813   Carpenter, J. H. 1965. The Accuracy of the Winkler Method for Dissolved Oxygen Analysis.

814   Limnol. Oceanogr. **10**: 135–140. doi:10.4319/lo.1965.10.1.0135

815   Cassar, N., B. A. Barnett, M. L. Bender, J. Kaiser, R. C. Hamme, and B. Tilbrook. 2009.

816   Continuous High-Frequency Dissolved O 2 /Ar Measurements by Equilibrator Inlet Mass

817   Spectrometry. Anal. Chem. **81**: 1855–1864. doi:10.1021/ac802300u

818   Codispoti, L. A., V. Kelly, A. Thessen, P. Matrai, S. Suttles, V. Hill, M. Steele, and B. Light.

819   2013. Synthesis of primary production in the Arctic Ocean: III. Nitrate and phosphate based

820   estimates of net community production. Prog. Oceanogr. **110**: 126–150.

821   doi:10.1016/j.pocean.2012.11.006

822   Craig, H., and T. Hayward. 1987. Oxygen Supersaturation in the Ocean: Biological Versus

823   Physical Contributions. Science (80-.). **235**: 199–202. doi:10.1126/science.235.4785.199

824   Danielson, S. L., O. Ahkinga, C. Ashjian, and others. 2020. Manifestation and consequences of

825   warming and altered heat fluxes over the Bering and Chukchi Sea continental shelves.

826   Deep. Res. Part II Top. Stud. Oceanogr. **177**. doi:10.1016/j.dsr2.2020.104781

827   Danielson, S. L., L. Eisner, C. Ladd, C. W. Mordy, L. Sousa, and T. J. Weingartner. 2017. A

828   comparison between late summer 2012 and 2013 water masses, macronutrients, and

829   phytoplankton standing crops in the northern Bering and Chukchi Seas. Deep. Res. Part II

830   Top. Stud. Oceanogr. **135**: 7–26. doi:10.1016/j.dsr2.2016.05.024

831   DeGrandpre, M., W. Evans, M. L. Timmermans, R. Krishfield, B. Williams, and M. Steele.

832   2020. Changes in the Arctic Ocean Carbon Cycle With Diminishing Ice Cover. Geophys.

833   Res. Lett. **47**. doi:10.1029/2020GL088051

834   Emerson, S. R., C. Stump, B. Johnson, and D. M. Karl. 2002. In situ determination of oxygen

835   and nitrogen dynamics in the upper ocean. Deep Sea Res. Part I Oceanogr. Res. Pap. **49**:

836   941–952. doi:10.1016/S0967-0637(02)00004-3

837   Emerson, S. R., C. Stump, and D. Nicholson. 2008. Net biological oxygen production in the

838   ocean: Remote in situ measurements of O 2 and N 2 in surface waters. Global Biogeochem.

839   Cycles **22**: n/a-n/a. doi:10.1029/2007GB003095

840   Emerson, S. R., B. Yang, M. White, and M. Cronin. 2019. Air-Sea Gas Transfer: Determining

841   Bubble Fluxes With In Situ N2 Observations. J. Geophys. Res. Ocean. **124**: 2716–2727.

842   doi:10.1029/2018JC014786

843   Eveleth, R., N. Cassar, R. M. Sherrell, H. Ducklow, M. P. Meredith, H. J. Venables, Y. Lin, and

844   Z. Li. 2017. Ice melt influence on summertime net community production along the

845   Western Antarctic Peninsula. Deep. Res. Part II Top. Stud. Oceanogr. **139**: 89–102.

846   doi:10.1016/j.dsr2.2016.07.016

847   Eveleth, R., M. L. Timmermans, and N. Cassar. 2014. Physical and biological controls on

848   oxygen saturation variability in the upper Arctic Ocean. J. Geophys. Res. Ocean. **119**:

849   7420–7432. doi:10.1002/2014JC009816

850   Garcia, H. E., and L. I. Gordon. 1992. Oxygen solubility in seawater: Better fitting equations.

851   Limnol. Oceanogr. **37**: 1307–1312. doi:10.4319/lo.1992.37.6.1307

852   Glueckauf, E. 1951. The Composition of Atmospheric Air, p. 3–10. *In* Compendium of

853   Meteorology. American Meteorological Society.

854   Grebmeier, J. M., B. A. Bluhm, L. W. Cooper, and others. 2015. Ecosystem characteristics and

855   processes facilitating persistent macrobenthic biomass hotspots and associated benthivory in

856   the Pacific Arctic. Prog. Oceanogr. **136**: 92–114. doi:10.1016/j.pocean.2015.05.006

857   Grebmeier, J. M., L. W. Cooper, H. M. Feder, and B. I. Sirenko. 2006. Ecosystem dynamics of

858   the Pacific-influenced Northern Bering and Chukchi Seas in the Amerasian Arctic. Prog.

859   Oceanogr. **71**: 331–361. doi:10.1016/j.pocean.2006.10.001

860   Grebmeier, J. M., S. E. Moore, J. E. Overland, K. E. Frey, and R. Gradinger. 2010. Biological

861   Response to Recent Pacific Arctic Sea Ice Retreats. Eos, Trans. Am. Geophys. Union **91**:

862   161. doi:10.1029/2010EO180001

863   Hamme, R. C., J. E. Berry, J. M. Klymak, and K. L. Denman. 2015. In situ O2 and N2

43

864   measurements detect deep-water renewal dynamics in seasonally-anoxic Saanich Inlet.

865   Cont. Shelf Res. **106**: 107–117. doi:10.1016/j.csr.2015.06.012

866 Hamme, R. C., N. Cassar, V. P. Lance, and others. 2012. Dissolved O2/Ar and other methods

867   reveal rapid changes in productivity during a Lagrangian experiment in the Southern Ocean.

868   J. Geophys. Res. Ocean. **117**: 1–19. doi:10.1029/2011JC007046

869 Hamme, R. C., and S. R. Emerson. 2004. The solubility of neon, nitrogen and argon in distilled

870   water and seawater. Deep. Res. Part I Oceanogr. Res. Pap. **51**: 1517–1528.

871   doi:10.1016/j.dsr.2004.06.009

872 Hamme, R. C., and S. R. Emerson. 2006. Constraining bubble dynamics and mixing with

873   dissolved gases: Implications for productivity measurements by oxygen mass balance. J.

874   Mar. Res. **64**: 73–95. doi:10.1357/002224006776412322

875 Harada, N. 2016. Review: Potential catastrophic reduction of sea ice in the western Arctic

876   Ocean: Its impact on biogeochemical cycles and marine ecosystems. Glob. Planet. Change

877   **136**: 1–17. doi:10.1016/j.gloplacha.2015.11.005

878 Hendricks, M. B., M. L. Bender, and B. A. Barnett. 2004. Net and gross O2 production in the

879   southern ocean from measurements of biological O2 saturation and its triple isotope

880   composition. Deep. Res. Part I Oceanogr. Res. Pap. **51**: 1541–1561.

881   doi:10.1016/j.dsr.2004.06.006

882 Hood, E. M. 1998. Characterization of Air-Sea Gas Exchange Processes and Dissolved Gas/Ice

883   Interactions Using Noble Gases. Massachusetts Institute of Technology & Woods Hole

884   Oceanographic Institution.

885 Hood, E. M., B. L. Howes, and W. J. Jenkins. 1998. Dissolved gas dynamics in perennially ice-

886   covered Lake Fryxell, Antarctica. Limnol. Oceanogr. **43**: 265–272.

887   doi:10.4319/lo.1998.43.2.0265

888   Izett, R. 2021. O2N2 NCP Toolbox.doi:10.5281/zenodo.4024925

889   Izett, R. W., R. C. Hamme, C. L. McNeil, C. C. Manning, A. Bourbonnais, and P. Tortell. 2021.

890   ΔO2/N2' as a new tracer of marine net community production: Application and evaluation

891   in the Subarctic Northeast Pacific and Canadian Arctic Ocean. Front. Mar. Sci.

892   Izett, R. W., and P. Tortell. 2020. The Pressure of In Situ Gases Instrument (PIGI) for

893   Autonomous Shipboard Measurement of Dissolved O2 and N2 in Surface Ocean Waters.

894   Oceanography **33**. doi:10.5670/oceanog.2020.214

895   Izett, R. W., and P. D. Tortell. 2021. ΔO2/N2′ as a tracer of mixed layer net community

896   production: Theoretical considerations and proof- of- concept. Limnol. Oceanogr. Methods

897   **19**: 497–509. doi:10.1002/lom3.10440

898   Juranek, L. W., and P. D. Quay. 2005. In vitro and in situ gross primary and net community

899   production in the North Pacific Subtropical Gyre using labeled and natural abundance

900   isotopes of dissolved O 2. Global Biogeochem. Cycles **19**: 1–15.

901   doi:10.1029/2004GB002384

902   Juranek, L. W., and P. D. Quay. 2010. Basin-wide photosynthetic production rates in the

903   subtropical and tropical Pacific Ocean determined from dissolved oxygen isotope ratio

904   measurements. Global Biogeochem. Cycles **24**: n/a-n/a. doi:10.1029/2009GB003492

905   Juranek, L. W., P. D. Quay, R. A. Feely, D. Lockwood, D. M. Karl, and M. J. Church. 2012.

906   Biological production in the NE Pacific and its influence on air-sea CO 2 flux: Evidence

907   from dissolved oxygen isotopes and O 2 /Ar. J. Geophys. Res. Ocean. **117**.

908   doi:10.1029/2011JC007450

909   Juranek, L. W., T. Takahashi, J. T. Mathis, and R. S. Pickart. 2019. Significant Biologically

910   Mediated CO 2 Uptake in the Pacific Arctic During the Late Open Water Season. J.

911   Geophys. Res. Ocean. **124**: 1–23. doi:10.1029/2018JC014568

912   Kaiser, J., M. K. Reuer, B. A. Barnett, and M. L. Bender. 2005. Marine productivity estimates

913   from continuous O 2 /Ar ratio measurements by membrane inlet mass spectrometry.

914   Geophys. Res. Lett. **32**. doi:10.1029/2005GL023459

915   Laws, E. A. 1991. Photosynthetic quotients, new production and net community production in

916   the open ocean. Deep Sea Res. Part A. Oceanogr. Res. Pap. **38**: 143–167. doi:10.1016/0198-

917   0149(91)90059-O

918   Lewis, K. M., G. L. Van Dijken, and K. R. Arrigo. 2020. Changes in phytoplankton

919   concentration now drive increased Arctic Ocean primary production. Science (80-.). **369**:

920   198–202. doi:10.1126/science.aay8380

921   Lockwood, D., P. D. Quay, M. T. Kavanaugh, L. W. Juranek, and R. A. Feely. 2012. High-

922   resolution estimates of net community production and air-sea CO 2 flux in the northeast

923   Pacific. Global Biogeochem. Cycles **26**. doi:10.1029/2012GB004380

924   Manning, C. C., R. H. R. Stanley, and D. E. Lott. 2016. Continuous Measurements of Dissolved

925   Ne, Ar, Kr, and Xe Ratios with a Field-Deployable Gas Equilibration Mass Spectrometer.

926   Anal. Chem. **88**: 3040–3048. doi:10.1021/acs.analchem.5b03102

927   Mathis, J. T., N. R. Bates, D. A. Hansell, and T. Babila. 2009. Net community production in the

928   northeastern Chukchi Sea. Deep Sea Res. Part II Top. Stud. Oceanogr. **56**: 1213–1222.

929   doi:10.1016/j.dsr2.2008.10.017

46

930   McNeil, C. L., B. D. Johnson, and D. M. Farmer. 1995. In-situ measurement of dissolved

931   nitrogen and oxygen in the ocean. Deep. Res. Part I **42**: 819–826. doi:10.1016/0967-

932   0637(95)97829-W

933   McNeil, C. L., D. Katz, R. Wanninkhof, and B. Johnson. 2005. Continuous shipboard sampling

934   of gas tension, oxygen and nitrogen. Deep. Res. Part I Oceanogr. Res. Pap. **52**: 1767–1785.

935   doi:10.1016/j.dsr.2005.04.003

936   Mesinger, F., G. DiMego, E. Kalnay, and others. 2006. North American Regional Reanalysis.

937   Bull. Am. Meteorol. Soc. **87**: 343–360. doi:10.1175/BAMS-87-3-343

938   Mordy, C. W., S. Bell, E. D. Cokelet, and others. 2020. Seasonal and interannual variability of

939   nitrate in the eastern Chukchi Sea: Transport and winter replenishment. Deep. Res. Part II

940   Top. Stud. Oceanogr. **177**: 104807. doi:10.1016/j.dsr2.2020.104807

941   Mordy, C. W., L. Eisner, K. Kearney, and others. 2021. Spatiotemporal variability of the

942   nitrogen deficit in bottom waters on the eastern Bering Sea shelf. Cont. Shelf Res. **224**:

943   104423. doi:10.1016/j.csr.2021.104423

944   NASA Goddard Space Flight Group; Ocean Ecology Laboratory; Ocean Biology Processing

945   Group. Moderate-resolution Imaging Spectroradiometer (MODIS) Aqua Chlorophyll Data;

946   2018 Reprocessing. NASA OB.DAAC, Greenbelt, MD, USA.

947   doi:data/10.5067/AQUA/MODIS/L3M/CHL/2018

948   Padin, X. A., M. Vázquez-Rodríguez, A. F. Rios, and F. F. Pérez. 2007. Atmospheric CO2

949   measurements and error analysis on seasonal air-sea CO2 fluxes in the Bay of Biscay. J.

950   Mar. Syst. **66**: 285–296. doi:10.1016/j.jmarsys.2006.05.010

951   Reuer, M. K., B. A. Barnett, M. L. Bender, P. G. Falkowski, and M. B. Hendricks. 2007. New

47

952   estimates of Southern Ocean biological production rates from O2/Ar ratios and the triple

953   isotope composition of O2. Deep Sea Res. Part I Oceanogr. Res. Pap. **54**: 951–974.

954   doi:10.1016/j.dsr.2007.02.007

955   Semiletov, I., A. Makshtas, S.-I. Akasofu, and E. L Andreas. 2004. Atmospheric CO 2 balance:

956   The role of Arctic sea ice. Geophys. Res. Lett. **31**: n/a-n/a. doi:10.1029/2003GL017996

957   Serreze, M. C., and J. Stroeve. 2015. Arctic sea ice trends, variability and implications for

958   seasonal ice forecasting. Philos. Trans. R. Soc. A Math. Phys. Eng. Sci. **373**.

959   doi:10.1098/rsta.2014.0159

960   Shadwick, E. H., B. Tilbrook, N. Cassar, T. W. Trull, and S. R. Rintoul. 2015. Summertime

961   physical and biological controls on O2 and CO2 in the Australian Sector of the Southern

962   Ocean. J. Mar. Syst. **147**: 21–28. doi:10.1016/j.jmarsys.2013.12.008

963   Shiozaki, T., A. Fujiwara, M. Ijichi, N. Harada, S. Nishino, S. Nishi, T. Nagata, and K.

964   Hamasaki. 2018. Diazotroph community structure and the role of nitrogen fixation in the

965   nitrogen cycle in the Chukchi Sea (western Arctic Ocean). Limnol. Oceanogr. **63**: 2191–

966   2205. doi:10.1002/lno.10933

967   Song, H., R. Ji, M. Jin, Y. Li, Z. Feng, Ø. Varpe, and C. S. Davis. 2021. Strong and regionally

968   distinct links between ice-retreat timing and phytoplankton production in the Arctic Ocean.

969   Limnol. Oceanogr. 1–11. doi:10.1002/lno.11768

970   Stammerjohn, S., R. Massom, D. Rind, and D. Martinson. 2012. Regions of rapid sea ice

971   change : An inter-hemispheric seasonal comparison. **39**: 1–8. doi:10.1029/2012GL050874

972   Stanley, R. H. R., J. B. Kirkpatrick, N. Cassar, B. A. Barnett, and M. L. Bender. 2010. Net

973   community production and gross primary production rates in the western equatorial Pacific.

974   Global Biogeochem. Cycles **24**. doi:10.1029/2009GB003651

975   Stroeve, J., and W. N. Meier. 2018. Sea Ice Trends and Climatologies from SMMR and SSM/I-

976   SSMIS, Version 3.doi:10.5067/IJ0T7HFHB9Y6

977   Teeter, L., R. C. Hamme, D. Ianson, and L. Bianucci. 2018. Accurate Estimation of Net

978   Community Production From O2/Ar Measurements. Global Biogeochem. Cycles **32**: 1163–

979   1181. doi:10.1029/2017GB005874

980   Thomson, J., and W. E. Rogers. 2014. Swell and sea in the emerging Arctic Ocean. Geophys.

981   Res. Lett. **41**: 3136–3140. doi:10.1002/2014GL059983

982   Toole, J. M., M. L. Timmermans, D. K. Perovich, R. A. Krishfield, A. Proshutinsky, and J. A.

983   Richter-Menge. 2010. Influences of the ocean surface mixed layer and thermohaline

984   stratification on Arctic Sea ice in the central Canada Basin. J. Geophys. Res. Ocean. **115**: 1–

985   14. doi:10.1029/2009JC005660

986   Tremblay, J.-É., and J. Gagnon. 2009. The effects of irradiance and nutrient supply on the

987   productivity of Arctic waters: a perspective on climate change. Influ. Clim. Chang. Chang.

988   Arct. Sub-Arctic Cond. 73–93. doi:10.1007/978-1-4020-9460-6_7

989   Tremblay, J. É., L. G. Anderson, P. Matrai, P. Coupel, S. Bélanger, C. Michel, and M. Reigstad.

990   2015. Global and regional drivers of nutrient supply, primary production and CO2

991   drawdown in the changing Arctic Ocean. Prog. Oceanogr. **139**: 171–196.

992   doi:10.1016/j.pocean.2015.08.009

993   Tremblay, J. É., S. Bélanger, D. G. Barber, and others. 2011. Climate forcing multiplies

994   biological productivity in the coastal Arctic Ocean. Geophys. Res. Lett. **38**: 2–6.

995   doi:10.1029/2011GL048825

49

996   Trull, T. W., P. Jansen, E. Schulz, B. Weeding, D. M. Davies, and S. G. Bray. 2019.

997   Autonomous Multi-Trophic Observations of Productivity and Export at the Australian

998   Southern Ocean Time Series (SOTS) Reveal Sequential Mechanisms of Physical-Biological

999   Coupling. Front. Mar. Sci. **6**: 1–17. doi:10.3389/fmars.2019.00525

1000   Wanninkhof, R. 2014. Relationship between wind speed and gas exchange over the ocean

1001   revisited. Limnol. Oceanogr. Methods **12**: 351–362. doi:10.4319/lom.2014.12.351

1002   Wassmann, P., and M. Reigstad. 2011. Future Arctic Ocean Seasonal Ice Zones and Implications

1003   for Pelagic-Benthic Coupling. Oceanography **24**: 220–231. doi:10.5670/oceanog.2011.74

1004   Weeding, B., and T. W. Trull. 2014. Hourly oxygen and total gas tension measurements at the

1005   Southern Ocean Time Series site reveal winter ventilation and spring net community

1006   production. J. Geophys. Res. Ocean. **119**: 348–358. doi:10.1002/2013JC009302

1007   Weiss, R. F., and B. A. Price. 1980. Nitrous oxide solubility in water and seawater. Mar. Chem.

1008   **8**: 347–359. doi:10.1016/0304-4203(80)90024-9

1009   Woolf, D. K., and S. A. Thorpe. 1991. Bubbles and the air-sea exchange of gases in near-

1010   saturation conditions. J. Mar. Res. **49**: 435–466. doi:10.1357/002224091784995765

1011